ELSEVIER

Chemical Geology 241 (2007) 62–87

CHEMICAL GEOLOGY
INCLUDING
ISOTOPE GEOSCIENCE

www.elsevier.com/locate/chemgeo

The impact of zircon–garnet REE distribution data on the interpretation of zircon U–Pb ages in complex high-grade terrains: An example from the Rauer Islands, East Antarctica

S.L. Harley *, N.M. Kelly

School of GeoSciences, University of Edinburgh, Edinburgh EH9 3JW, Scotland, UK

Accepted 17 January 2007

Abstract

The responsiveness of zircon to granulite metamorphism and post-peak fluid infiltration in polymetamorphic terranes has been investigated utilising a case study from the Rauer Islands of East Antarctica. Imaging (BSE, CL), textural analysis, in-situ ion microprobe trace element analysis of zircon, garnet, orthopyroxene, plagioclase and apatite, and ion microprobe oxygen isotope analysis of zircon, have been integrated to establish the event significance of c. 510 Ma zircon age domains that occur within and on c. 2840 Ma protolith magmatic zircons. Initial magmatic zircon is characterised by moderate Th/U (0.4–0.6) and elevated, steep HREE ($Yb_N/Gd_N = 20$). C. 510 Ma zircon domains feature lobate, cuspate and planar BSE and CL zones that have lower Th/U (to 0.05) and either decreased MREE, or decreased MREE and HREE. Metamorphic garnet, initially characterised by flat HREE, shows extensive replacement by orthopyroxene and plagioclase, accompanied by near-rim increases in HREE to values that are consistent with equilibrium between garnet rims and product orthopyroxene.

Zircon/garnet MREE–HREE distribution coefficients, D_{REE}, calculated using compositions of modified zircon domains coupled with both initial metamorphic garnet cores and rims are far removed from presently accepted equilibrium values, with the zircon MREE being strongly depleted relative to garnet. These D_{REE} indicate that the observed modification of zircon did not occur in response to the major high-grade metamorphic events recorded in the studied rock mineralogy, but instead occurred after the high-grade metamorphism. The zircon was 'blind' to these metamorphic events, but instead was responsive to a later post-peak fluid infiltration episode that shifted zircon $\delta^{18}O$ values downwards by some 3‰. The likelihood of 'blind' or unresponsive behaviour of zircon to high-grade metamorphism must be considered when reconstructing crustal histories and terrane scenarios based on U–Pb age data, and tested for using an integrated approach that includes in-situ REE and other trace element analysis of zircon and its potentially coexisting minerals.

Keywords: Zircon; REE; Ion microprobe; Granulite; Geochronology; Antarctica

1. Introduction

The interpretation of zircon age data in multiply-deformed and polymetamorphosed high grade terrains presents a significant problem in geochronology (Vavra et al., 1996; Schaltegger et al., 1999; Kelly

* Corresponding author. Tel.: +44 131 6504839.
E-mail addresses: Simon.Harley@ed.ac.uk (S.L. Harley), Nigel.Kelly@ed.ac.uk (N.M. Kelly).

0009-2541/$ - see front matter © 2007 Elsevier B.V. All rights reserved.
doi:10.1016/j.chemgeo.2007.02.011

and Harley, 2005). This arises because the response of zircon formed in one tectonothermal event, or preserved from older crustal precursors, to the imposition of later metamorphic events is now recognised as being highly variable even on the microscale. Although our capacity to precisely determine zircon U–Pb ages is now excellent, our incomplete understanding of the microscale physical and chemical processes that form or modify zircons in the metamorphic environment causes ambiguity in the interpretation of zircon U–Pb age populations (e.g. Friend and Kinny, 1995; Harley and Black, 1997). Such processes include subsolidus metamorphic reactions involving Zr-bearing silicate and accessory minerals (Fraser et al., 1997; Degeling et al., 2002), partial melting and melt crystallisation (e.g. Roberts and Finger, 1997; Schaltegger et al., 1999; Rubatto, 2002), dissolution and reprecipitation related to fluid infiltration (Pidgeon, 1992; Pidgeon et al., 1998; Harley et al., 1998; Vavra et al., 1999; Hoskin and Black, 2000), and annealing or 'healing' of zircon lattices to dissipate strain effects associated with ionic substitutions or rock deformation (McLaren et al., 1994; Hartmann et al., 1997; Schaltegger et al., 1999; Vavra et al., 1999; Hoskin and Black, 2000).

Ultimately, the reliable interpretation of age data in high grade terrains must be founded upon detailed textural analysis coupled with in-situ microanalysis that yields independent chemical criteria for constraining the processes that have affected or controlled zircon behaviour (Pidgeon, 1992; Hanchar and Miller, 1993; Roberts and Finger, 1997; Schaltegger et al., 1999; Vavra et al., 1999; Hoskin and Black, 2000; Rubatto, 2002; Kelly and Harley, 2005). The application of an integrated in-situ textural–chemical approach to zircon geochronology is illustrated here using a case study of zircon preserved in a garnet–pyroxene granulite from a metamorphosed Archaean layered igneous complex in the polymetamorphic Rauer Islands, east Antarctica. The initial impetus for this study was to address the problem of discriminating terranes and defining amalgamation events in this region (Harley and Fitzsimons, 1995; Harley et al., 1998; Harley, 2003), a recurring problem that is central to the analysis and understanding of all high-grade continental basement regions (e.g. Friend and Nutman, 1992; Friend and Kinny, 1995). However, of more general significance is the result that this integrated approach has yielded new insights relevant to the behaviour of zircon in ancient rocks subsequently affected by high grade metamorphism and later fluid access.

2. Geological context

The Rauer Islands are situated on the eastern coastline of Prydz Bay, East Antarctica (Fig. 1A). They are underlain by granulite facies orthogneisses and supracrustal sequences that collectively form a distinct high-grade region, the Rauer Terrane, located between the largely Neoproterozoic to Cambrian Prydz Belt to the south west and the Archaean to earliest Palaeoproterozoic Vestfold Block to the north east (Harley et al., 1995, 1998; Harley, 2003; Fig. 1A). Hence, given its present position the evolution of the Rauer Terrane is critical to understanding the amalgamation of East Antarctica, and particularly the relative importance of c. 1000 Ma and c. 530–510 Ma tectonothermal events in welding together the various Archaean and Proterozoic crustal blocks (Hensen and Zhou, 1995; Zhao et al., 1995; Carson et al., 1996; Hensen and Zhou, 1997; Fitzsimons, 2000; Boger et al., 2001; Harley, 2003).

The Rauer Terrane contains both Archaean and Proterozoic crustal components (Kinny et al., 1993; Fig. 1B). Archaean orthogneisses and their precursors, ranging in age between 2804 Ma and 3550 Ma (Kinny et al., 1993; Harley et al., 1998), were subjected to high-grade metamorphism prior to 2500 Ma and subsequently intruded by several generations of mafic dykes, now deformed and metamorphosed to granulite facies assemblages (Sims et al., 1994; Harley et al., 1995). Late Mesoproterozoic sediments and felsic intrusives underwent granulite facies deformation in the c. 1000 Ma Rauer tectonic event (Kinny et al., 1993; Harley et al., 1998). Both Archaean and Proterozoic gneiss suites were variably overprinted at 530–510 Ma by amphibolite and granulite facies high strain zones (Sims et al., 1994) linked with the Prydz Belt tectonism (Prydz Tectonic Event) now recognised as a major tectonothermal episode in East Antarctica (Fitzsimons, 2000; Boger et al., 2001).

A key question that emerges from this complex history is whether the Prydz Belt tectonism was responsible for the high-grade amalgamation and interleaving of distinct Archaean and Mesoproterozoic lithotectonic units that had different crustal histories (Hensen and Zhou, 1997), or merely reworked a mixed package of Archaean–Proterozoic gneisses that had been assembled previously in and shared the c. 1030–1000 Ma Rauer tectonic event (Kinny et al., 1993; Harley et al., 1998). In order to discriminate between these alternatives it is necessary to establish whether the Archaean gneisses were reworked in both the Rauer and Prydz tectonic events, and determine the grade and effects of the Prydz tectonic event itself.

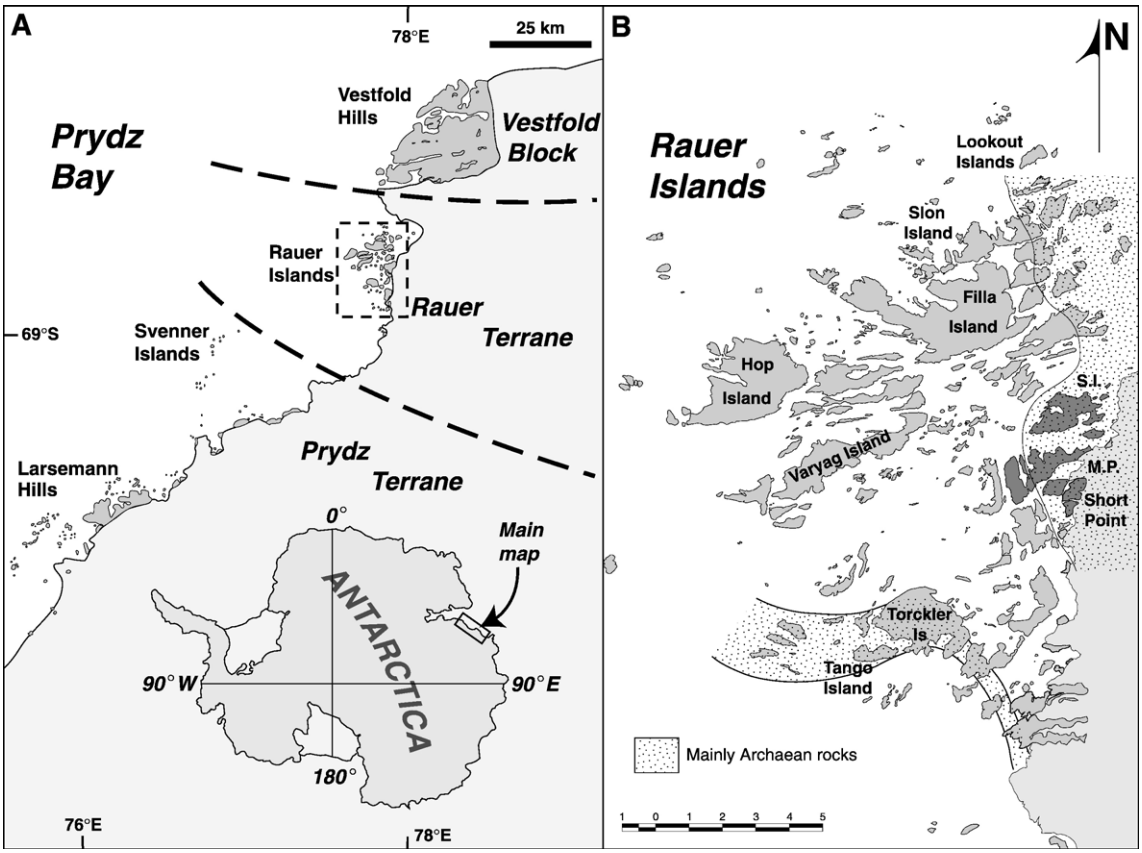

Fig. 1. (A) Map of the Prydz Bay region of East Antarctica, modified after Harley et al. (1995), showing the position of the Rauer Terrane relative to the Archaean Vestfold Block and the dominantly Neoproterozoic–Cambrian Prydz Terrane. Inset: map of Antarctica with the position of the main map. (B) Map of the Rauer Group of islands, showing the approximate location of predominantly Archaean rocks; Scherbinina Island (SI), Mather Peninsula (MP) and Short Point are shaded darkly.

2.1. Archaean Relics in the Rauer Terrane: The Scherbinina Layered Complex

Within the Rauer Islands there are a number of late low-strain zones in which Archaean layered igneous intrusive bodies can be recognised with their original structures preserved with relatively minor modification (Harley and Fitzsimons, 1995; Harley et al., 1995, 1998). Such layered complexes provide an opportunity for examining how Archaean magmatic zircons have responded to the later metamorphic events, and potentially evaluating whether the Archaean rocks underwent metamorphism in both the c. 1000 Ma and 530–510 Ma events or not.

The Scherbinina Layered Complex (SLC: Harley et al., 1998; Fig. 1B), which occupies an area of 0.1 km^2 at the eastern extremity of Scherbinina Island, is the best studied of these layered meta-igneous bodies. The SLC comprises gabbro, ferrogabbro, ferrodiorite and ultramafic igneous precursors metamorphosed to granulite grade and deformed in several events both prior to and after intrusion by later mafic and felsic dyke suites (Snape, 1997; Harley et al., 1998). Despite this, the SLC preserves relic igneous features including rhythmic modal and graded layering, ophitic and chadacryst textures, (meta-)gabbro pegmatite lenses, and coarse segregations or schlieren that represent late-stage conduits, differentiates and accumulated crystals (Snape, 1997).

SHRIMP U–Pb dating of zircons from two such rocks, one a ferrogabbro pegmatite lens (RI43) and the other a quartz-bearing schlieren (RI15), has yielded a magmatic age of 2844±6 Ma for the SLC (Harley et al., 1998; full data presented in Supplementary Data Table 1). This age was based on concordant and near-concordant zircon analyses that lie at the upper end of a discordia defined by a spread in zircon U/Pb analyses (Fig. 2). The discordia based on RI43 has a lower intercept, at 512±12 Ma, that is coincident with the age of 511±10 Ma defined by near-concordant

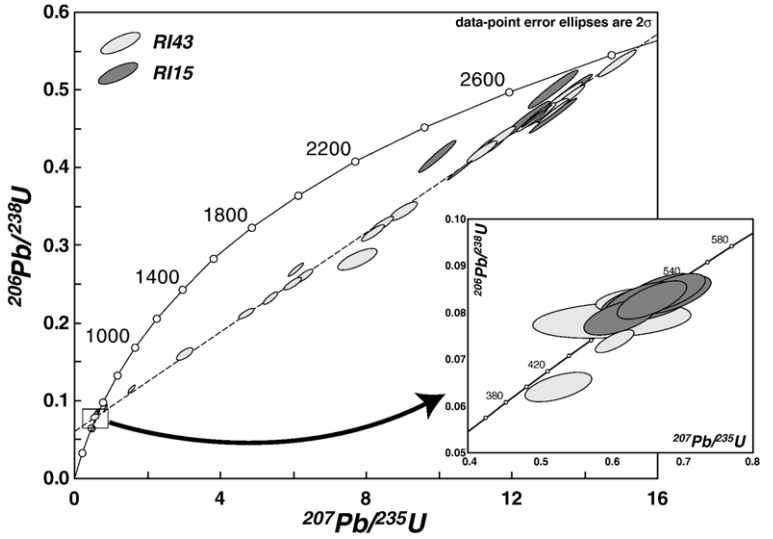

Fig. 2. Concordia diagram showing the collective SHRIMP zircon U–Pb data for samples RI15 (solid ellipses) and RI43 (open ellipses) from the Scherbinina Layered Complex. Data from Harley et al. (1998), recalculated and plotted the software of Ludwig (1999, 2001). Note extensive Pb loss along a discordia from c. 2840 Ma to lower intercept of c. 510 Ma that coincides with the U–Pb ages of concordant zircon domains in each rock.

multifaceted zircon grains and modified zircon domains in RI15.

The partially- to fully reset zircon ages were correlated by Harley et al. (1998) with lobate and cuspate 5–30 μm scale zircon micro-domains distinguished by high and variable cathodoluminescence (CL) response. Harley et al. (1998) also correlated these texturally modified domains in sample RI15 with changes in the zircon REE compositions from primary igneous REE patterns to patterns characterised by relative depletions in the MREE, and suggested that this behaviour reflected the response of zircon to fluid infiltration subsequent to the high-grade metamorphic events. However, that preliminary study did not present complementary REE data for the other phases in RI15 to constrain the relative timing of trace element change in the zircons and so test this model.

Therefore, an important aspect of the present study is to further evaluate how the c. 510 Ma partial to total resetting of c. 2840 Ma zircon has occurred, and under what conditions, using independent chemical information. In this work we report new micro-analytical data, including major and trace element analyses and Xray maps, of zircon and all other modally important phases in RI15. These data, interpreted in concert with recent estimates of the equilibrium distribution of REE and Y between zircon, garnet and orthopyroxene, allow the chemical–textural evolution of zircon in RI15 to be traced and, most importantly, linked with the mineral assemblage and reaction history of the rock. Using this approach we demonstrate that zircon in this case has been unresponsive to the metamorphic events that firstly produced garnet and were subsequently responsible for the reaction of garnet under high-temperature conditions. Instead, and as provisionally suggested by Harley et al. (1998), zircon in this case study has been highly responsive to late-stage, post-peak metamorphic fluid ingress at or about 530–510 Ma.

3. Metamorphic petrology of RI15

Sample RI15, described previously in Harley et al. (1998), is a granulite facies metamorphic rock dominated by modally abundant garnet (c. 40–50 modal %) that occurs as 1–3 mm diameter porphyroblasts set in quartz (15–20%). The other minerals in this metaferrodiorite are orthopyroxene (5–10%), plagioclase (15–25%), apatite (3%), magnetite (2%), sulphides (pyrite, chalcopyrite, pyrrhotite, pentlandite) and zircon (1–2%).

Initial metamorphic grain contacts between garnet and quartz in RI15 are almost entirely replaced by layered coronas consisting of granoblastic to blocky orthopyroxene (0.2–1 mm) preferentially developed adjacent to quartz, surrounding granoblastic plagioclase that occurs preferentially adjacent to garnet (Figs. 3A and 4A). The initially subhedral garnet porphyroblasts now preserve lobate–cuspate and resorbed grain edges with coronal plagioclase, indicative of reaction and resorption. The coarse, texturally equilibrated orthopyroxene–plagioclase

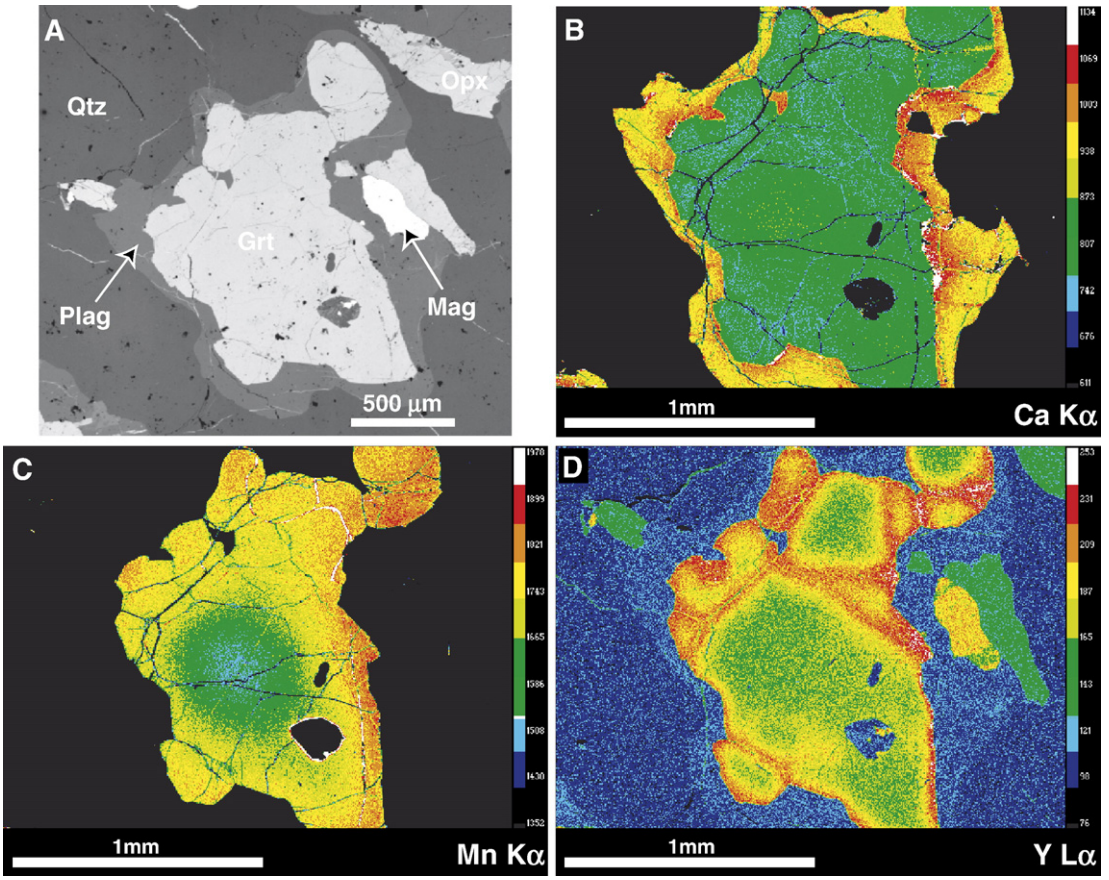

Fig. 3. BSE image (A) and Xray intensity (element) maps (b, c and d) for a garnet from sample RI15. (B) Element map for Ca: only a small core area of relatively higher Ca is preserved in the garnet. (C) Element map for Mn: a c. 500 μm diameter low-Mn modified core is preserved, surrounded by an extensive broad rim characterised by higher Mn. (D) Element map for Y: note the restriction of elevated Y to narrow (50–100 μm) zones concentric with the resorbed rim of the garnet or traversing along grain boundaries/sealed fractures within the garnet cluster.

domains occur only on garnet, and are ambivalent to the presence of the other phases (apatite, magnetite, sulphides, zircon) in RI15.

As documented by Harley et al. (1998), the granulite facies metamorphic evolution of RI15 involved formation of the initial garnet–quartz (+ orthopyroxene) assemblage, followed by reaction under granulite facies conditions to produce the assemblage garnet–orthopyroxene–plagioclase–quartz, with plagioclase+orthopyroxene forming at the expense of garnet+quartz (Harley et al., 1998). Mapping and area counting of 3 thin sections of RI15 indicate that 25 modal % of the initial garnet has been consumed in this reaction.

On the basis of garnet–orthopyroxene Fe–Mg–Al thermobarometry and garnet–orthopyroxene–plagioclase–quartz barometry Harley et al. (1998) calculated conditions of $P>8$ kb and $T\approx820$ °C for the initial plagioclase-absent garnet–orthopyroxene–quartz assemblage, assuming core garnet compositions to have been in equilibrium with a small amount of the preserved orthopyroxene. Conditions of $P\approx8$ kb and $T\approx780$ °C were calculated for the garnet–orthopyroxene–plagioclase–quartz assemblage using a typical garnet rim composition.

The temperature conditions relevant to the formation/equilibration of the orthopyroxene–plagioclase coronas between garnet and quartz in RI15 have been recalculated using more recent garnet–orthopyroxene thermometers (Ganguly et al., 1996; Aranovich and Berman, 1997) and a significantly larger analytical database (c. 340 analyses) that includes several garnet and orthopyroxene electron microprobe traverses. These data show that whilst garnet is strongly zoned between the compositions noted above, with major rimward increases in Mn and Fe coupled to decreases in Ca ($Alm_{59}Prp_{14}Grs_{24}Sps_3$ to $Alm_{67}Prp_{12}Grs_{15}Sps_6$; see mineral chemistry section), the coronal orthopyroxene is unzoned ($X_{Mg}=36.3$; $Al_2O_3=0.83$ wt.%) and

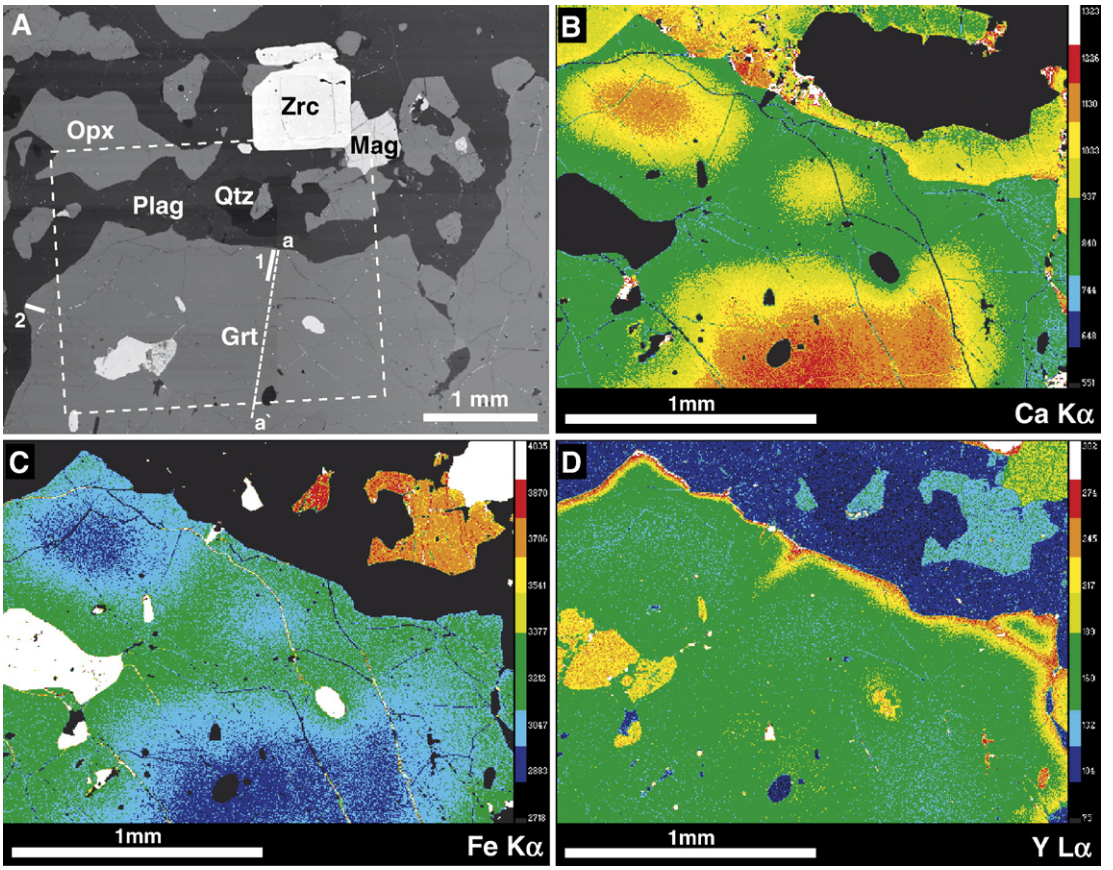

Fig. 4. BSE (A) and Xray intensity (element) maps (B, C and D) of the large garnet area and adjacent zircon grain #1 in RI15. (A) BSE image showing the general garnet-breakdown texture. Area mapped for elemental zoning is shown in the dashed box. Electron microprobe traverse line relevant to Fig. 7 is shown (a–a′). This traverse is adjacent to SIMS traverse 1 (also seen as black dots on Fig. 9B and C). SIMS traverse 2 lies to the left of the mapped field of view. (B) Element map for Ca: note preservation of large core area interior to a broad low-Ca zone that is overall concentric with the resorbed garnet rim. More restricted areas of high Ca also occur, along traverse line a–a′ and in the top left of the grain. (C) Element map for Fe: shows antithetic features to Ca — high Fe occurs in the same regions where low Ca is measured. (D) Element map for Y: as for Fig. 8, the marked (at least 3-fold) increase in Y is localised to within 100 mm of the resorbed garnet rim, and is concentric with the rim or contained within fractures (e.g. right side of garnet).

plagioclase shows only minor zoning (An_{38} near Opx to $An_{41–42}$ near Grt; see Supplementary Data tables). The resultant temperature estimates based on garnet rims coupled with orthopyroxene are $T=810\pm45$ °C (Fe–Mg thermometry: Ganguly et al., 1996) and $T=777\pm36$ °C (Fe–Al thermometry: Aranovich and Berman, 1997) at $P=8\pm1$ kb. These are consistent with those previously estimated, and confirm the interpretation that the resorption of initially high-grossular garnet (Grs 24 mol%) progressed under granulite facies conditions.

4. Zircon petrography

Zircons from both samples reported by Harley et al. (1998) have been examined using BSE and CL imagery (Fig. 5). Those in RI15 have been observed in-situ in thin section, whereas zircon separates from RI43 (ferrogabbro pegmatite lens) have been imaged in their polished SHRIMP ion probe epoxy mount. Grains and mineral textures were imaged in detail using the Phillips XL30 Scanning Electron Microscope (SEM) located at the Grant Institute of Earth Science, University of Edinburgh. Cathodoluminescence (CL) images were obtained at 15 kV and ~30 μA and Backscattered Electron (BSE) images were obtained at 20 kV and 40–50 μA. The textural features observed in each case are similar, and are summarised collectively below.

The zircons, whether observed as grain separates or in-situ, occur as 100–500 μm long, randomly orientated, euhedral to subhedral prisms with typical length:width aspect ratios between 2:1 and 3:1 (Fig. 5f, k). These

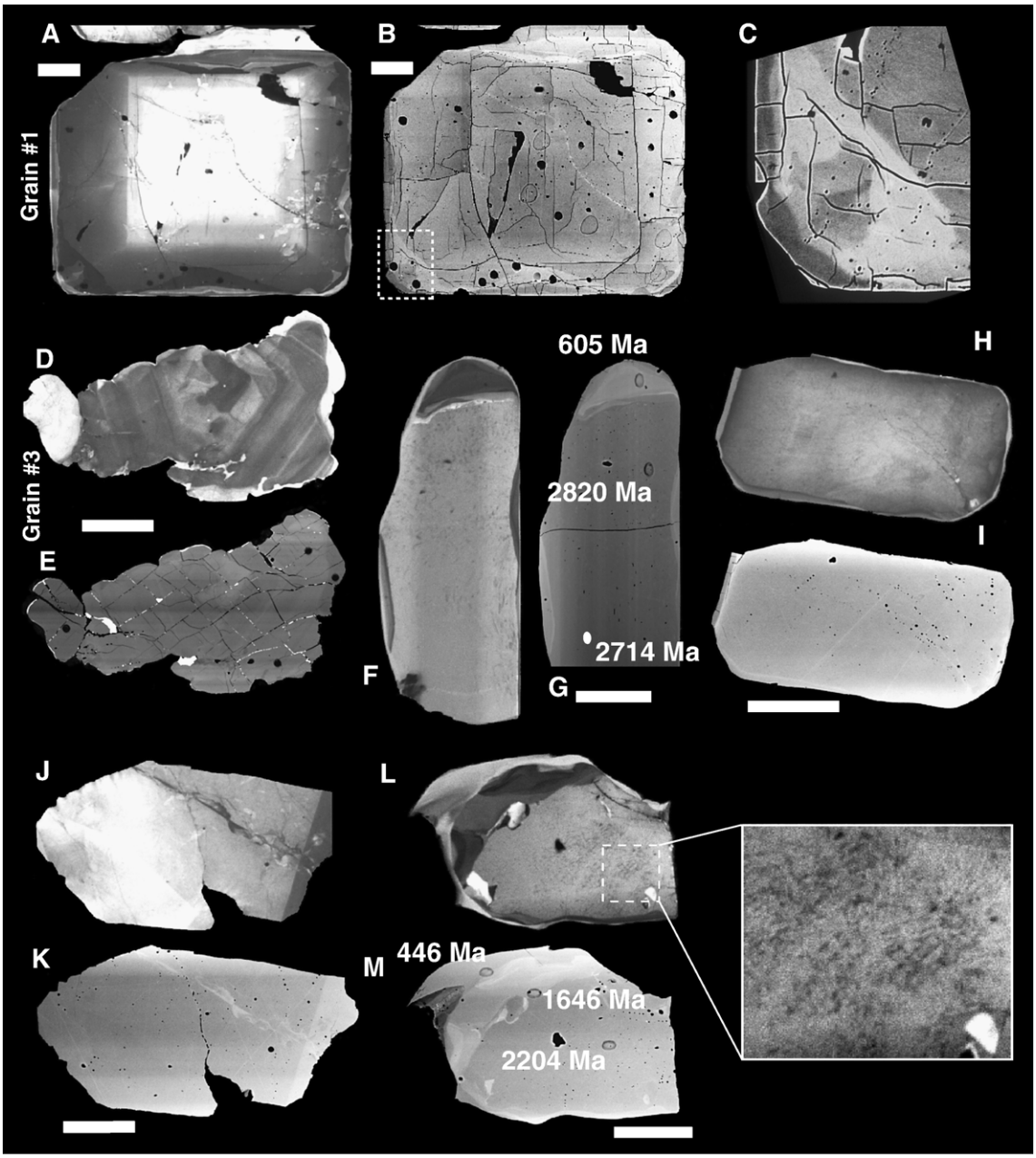

Fig. 5. Cathodoluminescence (CL: a, d, f, h, j, l) and backscattered electron (BSE: b, c, e, g, i, k, m) images of selected zircon grains from RI15 (a–e) and RI43 (f–m). Images a, b and c are of RI15 grain #1, which is analysed and described in detail. Large elliptical pits seen in b are sites of oxygen analysis; smaller round pits (shown as black dots) are sites of REE analysis for this grain. Images d and e are of RI15 grain #3. See text for description and discussion. Scale bars are 100 μm.

prisms have square cross-sections dominated by (100) and (101) faces (Fig. 5A, B), with short (110) diagonal faces developed along the prism face joins (Fig. 5C). Pyramidal terminations and tips are developed at the ends of otherwise prismatic grains (Fig. 5J) and may form the bulk of grains that are assumed to have been sectioned near such terminations (Fig. 5D).

The originally euhedral crystal shapes of the zircons have in most cases been slightly modified by rounding of prism edges, tips and terminations (Fig. 5G, I, M), whilst in some cases pinching and rounding of prism faces has occurred (Fig. 5H, J). More extensive modifications to the morphology of some zircon grains are observed, and include corrosion leading to cuspate

grain edges (Fig. 5L, M), rounded to irregular grains (Fig. 5D, F), and occasional grains that are both irregular and cuspate.

Five texturally-defined zircon domain types are distinguished based on these morphological features in combination with the internal and grain edge features revealed by both BSE and CL imaging:

1) The dominant magmatic zircon type, characterised by first-order prisms (e.g. Koschek, 1993; Corfu et al., 2003). This preserves planar to gradational CL/BSE zoning parallel to the prism faces (Fig. 5A, B, G) and only minor or negligible oscillatory zoning.
2) Interior areas of several prismatic zircon grains in which gradational magmatic zoning is not preserved but in which an irregular to 'spongy' or 'swirly' texture, best seen in CL (RI43: Fig. 5J, L — highlighted box), is observed. This type of texture is developed in grains that are traversed by micro-fractures as described in texture (5) below.
3) Lobate and cuspate, 5–60 μm width micro-domains that have dark CL and bright BSE responses (Fig. 5A, B, C, G, L, M). These occur along prism faces, at grain tips and in triangular zones where prism faces meet (e.g. Fig. 5A, B, C, F), and appear to invade and transgress previously formed gradational (Fig. 5A, B) zoning. In detail these domains are succeeded outwards at grain edges by 2–25 μm width cuspate to planar zones (Fig. 5B) that are brighter in CL and dark in BSE (Fig. 5C, F, H, L). The interior bright BSE zones are usually broader, and have been focussed on in this study to examine changes in zircon composition.
4) Less common pyramidal zircon and zircon tips that preserve fine-scale (5–10 μm) curved/irregular to oscillatory and planar zoning, best seen in CL (Fig. 5D). In detail, lobate oscillations are succeeded by more planar zones further from the boundary with type (1) zircon, and both varieties of oscillatory zone are terminated by narrow (2–5 μm) bright CL zones at grain margins. In grains where both types of texture are seen, type (4) zones with curved/irregular to oscillatory and planar zoning transgress gradationally zoned (type (1)) domains or develop on lobate to cuspate type (3) domains that are invasive into type (1).
5) Sealed microfractures and microfracture arrays that propagate into and traverse gradationally zoned zircon domains (type (1)). That these fractures are sealed can be demonstrated by examining the CL and BSE images of Fig. 5. The fractures are characterised by dark CL (Fig. 5A, J, L) and bright BSE (Fig. 5B, K, M) responses, and by concentrations of trails of 1–10 μm diameter holes (Fig. 5B, C, K, M), interpretable as former fluid inclusion bubbles. These bubble trails do not extend to the present grain edges but instead terminate at the interface between the bright BSE lobate domains (3) and less disturbed zircon interiors. In some cases, bright BSE flames or filaments can be seen emanating from this internal boundary into the zircon of type (1).

Type (1) zircon is interpreted on the basis of its dominance and its occasional preservation of euhedral zoning features to be original magmatic zircon grown in the SLC and accumulated in RI15. Further geochemical evidence in support of this will be presented and evaluated below. The remaining four zircon textural domains and features are superimposed on and reflect disturbance of this zircon, which generally shows signs of limited corrosion (Fig. 5F, K, M) and little textural evidence for overgrowth. The only case in which new zircon growth may be inferred is in relation to the type (4) zircon that occurs on pyramidal grain tips.

5. Mineral trace and major element chemistry

5.1. Analytical methods

Zircon and apatite U–Pb, Th, Y, Hf, Ti and REE, and garnet, plagioclase and orthopyroxene major element Y, Ti, Zr and REE data, have been obtained in-situ from selected but representative textural domains in which the features described above are well-preserved.

SIMS analysis of zircon, garnet, orthopyroxene, plagioclase, apatite and magnetite was carried out at the NERC Ion Microprobe Facility, University of Edinburgh, using a Cameca ims-4f ion microprobe. Analytical and correction procedures follow those outlined by Hinton and Upton (1991). Minerals were analysed using a 14.5 keV primary beam of O^- at ~5 nA primary current focussed to a 15–20 μm spot, with secondary ions measured at 120 V offset (zircon) and 75 V offset (garnet and orthopyroxene). For each analysis 10 cycles were made through the masses of interest. Ion yields were calculated using the NIST SRM-610 glass standard and concentrations were referenced against Si, as determined by electron microprobe. For zircon, corrections were made for $ZrSiO^+$ overlap on $^{138}Ba^+$, $^{139}La^+$, $^{140}Ce^+$ and $^{141}Pr^+$ using count rates measured at mass 134. Analytical reproducibility during and between analytical periods was tested using analyses of the 91500, SL1 and SL13 zircon standards (zircon analysis) and 'ddigrt' standard (garnet and orthopyroxene analysis). Representative and average REE data are summarised in Tables 1 and 2, whilst full ion microprobe

data can be found in Supplementary Data Tables 2, 3 and 4.

Garnet, orthopyroxene and plagioclase were analysed for their major elements at texturally-constrained sites and along line traverses using the Cameca SX-100 5 spectrometer electron microprobe at EMMAC, Grant Institute of Earth Science, University of Edinburgh. Operating conditions were 20 kV and 20 nA absorbed sample current, with 30 s counting times on the elemental peaks. Analyses were reduced using Cameca PAP software (Pouchou and Pichoir, 1984), and recalculated following a user-defined algorithm (SLH) that balances charge and sites in garnet excluding the tetrahedral (Si) site, as Si has been observed to be subject to systematic analytical/data reduction errors in the PAP procedures as used on the SX100 instrument. Representative electron microprobe data are presented in Table 3, with full data presented in Supplementary Data Tables 5, 6 and 7. Xray intensity (element) maps of Ca, Mg, Fe, Mn and Y (Figs. 4 and 5) were obtained for garnet and adjacent minerals using the Cameca SX-100 under operating conditions of 20 kV and 200 nA absorbed sample current, with step sizes of 2–3 μm, dwell times of 100 ms, and each map collected twice, leading to typical collection times of 8–12 h per map set.

5.2. Zircon chemistry and REE variations

Three zircon grains have been analysed for trace elements. Grain #1 displays the greatest range in textures and so has been analysed in greatest detail (18 trace element analyses, 5 oxygen isotope analyses). Distinct textural domains in prismatic grain #2 (5 analyses) and cuspate grain #3 (6 analyses) have also been analysed.

5.2.1. Unmodified gradationally zoned magmatic zircon (type (1))

Unmodified or little modified magmatic zircons of textural type (1) show half an order of magnitude variation in their overall REE abundances (Table 1; Fig. 6A), consistent with variations in Y between 400 and 2000 ppm. Despite this, the REE patterns are similar in terms of parameters such as Yb_N/Gd_N (14–25) and Eu/Eu* (0.13–0.16).

Type (1) zircon in grain #1 shows core to rim chemical variation correlated with the CL and BSE responses described above. The chemical zonation is characterised by core to rim increases in HfO_2 (1.33 to 2.0 wt.%), U (cores 150–220 ppm, outer zones 600–900 ppm), Th (cores 60–100 ppm, outer zones 300–350 ppm), Y and HREE (Figs. 6A and 7A, B). These changes in abundances lead to rimward increases in Yb_N/Gd_N (14 to 25) and Ce/Ce* (7 to 14), and slight decreases in Eu/Eu* (0.16 to 0.13) and Th/U (0.52 to c. 0.45) that are correlated with HfO_2, U, and BSE brightness (Fig. 7C).

In view of these consistent chemical variations, the type (1) zircons are considered to reflect crystallisation from melt that evolved to higher Hf, U, Th and REE with fractionation. The averaged zircon REE pattern calculated using all unmodified zircon domains weighted according to their relative modal proportions in grains #1 and #2 has Gd_N of c. 120–160 and Yb_N/Gd_N of c. 15–17, Ce/Ce*=11–16, Eu/Eu*=0.14–0.15, $Sm_N/Nd_N = 3.8–4.4$, $Th/U = 0.48–0.5$ and HfO_2=1.72 wt.%. These trace element features, which are relatively robust to the method of averaging used because of the high proportion of type (1) 'core', will be used for later REE calculations involving other mineral and whole rock SLC data.

5.2.2. Texturally modified zircon domains (2), (3), (4) and (5)

Type (2) textural domains in RI43, showing spongy or swirly disturbed CL patterns (Fig. 5H, J, L) are characterised by high Th/U (0.6–0.9) caused by relatively low U (60–120 ppm) rather than high Th (50–80 ppm). In RI15 similarly disturbed core zircon (grain #1; RI15-2: Th/U=0.71) has slightly lowered HfO_2 (=1.48 wt.%), Gd_N (=22) and Yb_N/Gd_N (=10.2), and elevated Ce/Ce* (=16) (Figs. 6A and 7). These chemical changes are distinct from those associated with the zoning reported above for unmodified type (1) zircon textural domains.

Bright CL domains with little internal structure, interpreted as type (2) domains, have also been observed associated with lobate to oscillatory zoned grain tip domains (textural type (4)) in RI15 grain #3 and grain #1 (4 analyses). These domains have Th/U (0.53) similar to type (1) zircon, but with both U (99–162 ppm) and Th (51–95) lowered relative to that unmodified zircon (Fig. 7B). Averaged HfO_2 (=1.58 wt.%), Gd_N (=33) and Yb_N/Gd_N (=9) are all lower than type (1) zircon, and Sm_N/Nd_N (=5.2) and Ce/Ce* (=28) are elevated (Fig. 6C).

Type (3), bright BSE/dark CL cuspate/lobate zones have been analysed from grain #1 (5 analyses). They are characterised by elevated HfO_2 (1.8–2.3 wt.%) and U (1000–1600 ppm), and decreased MREE (e.g. Gd_N=7–70; Sm_N=2–24) and Th (40–120 ppm) compared with type (1) zircon (Figs. 6B and 7B, C). These modified domains have REE patterns that are more highly fractionated (average Yb_N/Gd_N=89; Yb_N/Nd_N=467

Table 1
Average and representative zircon ion microprobe data for RI15

	Average zrc type (1) (Gr1)	Average zrc type (1) (Gr2)	Average zrc type (2) (All)	Average zrc type (3) (All)	Average zrc type (4) (All)	RI15-9 (T1-Gr1)	RI15-2 (T1-Gr1)	RI15-06-1 (T1-Gr1)	RI15-06-7 (T2-Gr3)	RI15-8 (T3-Gr1)	RI15-6 (T3-Gr1)	RI15-14 (T4-Gr2)	RI15-06-8 (T4-Gr3)	RI15-06-3 (T4-Gr1)
Si	140,230	140,230	147,083	–	145,370	–	–	140,230	140,230	–	–	–	140,230	140,230
P	181	0	121	–	96	–	–	0	120	–	–	–	81	50
Ca	20	31	97	–	15	–	–	31	286	–	–	–	25	1
Y	1467	519	205	493	163	1930	937	416	277	696	–	208	154	115
Zr	548,243	556,973	510,818	572,250	535,773	581,000	–	544,920	527,490	558,000	–	577,000	534,290	520,290
Ti	3.12	1.45	6.08	–	6.36	–	–	1.45	6.08	–	–	–	11.30	1.42
Ba	0.25	0.23	2.00	–	0.27	–	–	0.23	5.61	–	–	–	0.42	0.16
La	8.24	4.95	5.13	7.68	2.99	8.22	0.89	0.24	19.13	14.36	0.17	8.44	0.38	0.16
Ce	75.28	33.03	21.04	18.76	14.34	42.11	12.45	33.77	39.99	32.49	7.18	21.22	17.63	2.72
Pr	4.01	0.51	3.12	2.12	1.01	3.11	1.80	0.60	10.38	8.07	0.11	0.93	1.57	0.20
Nd	22.07	6.14	4.01	4.81	1.97	10.50	5.79	2.25	12.31	12.51	0.35	2.43	2.34	0.35
Sm	47.27	7.70	9.84	7.72	4.25	54.22	39.12	6.37	19.81	23.27	1.77	3.50	6.63	2.37
Eu	16.18	3.88	7.13	2.84	4.31	19.11	16.96	3.15	10.63	6.11	1.43	2.30	6.48	5.30
Gd	191	45	33	28	21	234	156	36	57	70	7	20	26	28
Tb	368	98	61	72	42	471	263	75	87	145	33	42	47	49
Dy	674	206	95	150	70	869	470	162	133	267	76	80	79	65
Ho	1048	360	130	281	95	1410	686	280	174	464	159	128	92	62
Er	1746	631	195	570	142	2448	1108	503	252	875	278	201	118	72
Tm	2368	922	222	985	194	3393	1116	754	299	1372	583	305	144	78
Yb	2863	1141	277	1453	234	4117	1592	931	351	1877	954	394	163	87
Lu	4163	1747	413	2625	356	5844	2339	1483	522	3123	2003	597	247	152
HfO^2	1.79	1.73	1.58	2.14	1.87	2.04	1.48	1.72	1.76	2.17	1.98	1.98	1.97	1.97
Th	190	70	69	76	30	329	65	64	95	127	41	30	39	19
U	440	165	128	1296	459	704	91	129	162	1180	1021	548	478	333
Th/U	0.49	0.43	0.53	0.06	0.07	0.47	0.71	0.50	0.59	0.11	0.04	0.05	0.08	0.06
Yb_N/Gd_N	19.39	31.03	10.87	92.59	14.57	21.29	12.38	31.16	7.52	32.35	162.16	23.75	7.65	3.81
Yb_N/Dy_N	6.50	8.32	4.39	15.91	4.95	7.07	5.06	8.60	3.93	10.52	18.76	7.41	3.07	1.99
Y_N/Ho_N	0.05	0.05	0.06	0.06	0.06	0.05	0.05	0.05	0.06	0.05	–	0.06	0.06	0.07
Sm_N/Nd_N	14.03	5.44	15.87	7.11	10.15	15.89	20.79	8.70	4.95	5.72	15.39	4.43	8.74	20.72
Eu*	0.14	0.15	0.35	0.21	0.34	0.13	0.17	0.15	0.28	0.13	0.32	0.20	0.40	0.35
Ce*	18.02	32.60	28.10	15.31	14.27	7.43	9.26	79.83	2.71	2.90	50.79	4.53	18.11	14.80

Note: All concentration values in ppm except HfO_2 (wt%).

Table 2
Representative mineral ion microprobe data for RI15

	Grt core average	Grt rim average	RI15g4	RI15g7	ri15g22	RI15g1b	ri15g1a	Opx average	Plag	Apt average
Si	176,816	177,062	176,690	176,690	177,620	176,690	176,690	224,370	257,090	970
P	40	62			38		35	6.45	43.9	194,757
Ca	49,920	43,470	46,189	44,463	41,049	44,664	50,213	7424	44,603	226,967
Y	570	1850	61	77	75	145	230	33.8	0.54	757
Zr	17	10	0	0	0	0	0	3.21	0.01	–
Ti	207	59	2062	1510	1304	596	515	131	7.29	–
Sr	0.13	0.22	8.10	12.90	11.10	17.04	17.54	0.06	25.2	–
Nb	0.01	0.01	0.01	0.01	0.02	0.01	0.02	0.01	–	–
Ba	0.01	0.02	0.02	0.08	0.01	0.02	0.00	0.01	18.6	–
La	0.05	0.04	0.04	0.03	0.02	0.06	0.04	0.08	17.1	652
Ce	0.80	0.45	0.45	0.54	0.40	0.81	0.79	0.33	21.4	1650
Pr	0.57	0.31	0.45	0.30	0.32	0.53	0.64	0.09	1.65	218
Nd	10.93	7.28	9.18	7.68	7.38	11.29	11.66	0.88	6.08	1110
Sm	14.38	14.10	17.76	15.56	13.52	18.44	13.22	0.64	0.48	242
Eu	2.69	1.79	1.99	2.14	1.84	3.09	2.83	0.05	2.03	16
Gd	43	61	71	66	55	46	42	1.55	0.18	221
Tb	14	23	26	22	21	13	14	0.56	0.05	34
Dy	111	254	288	227	204	114	111	5.50	0.13	211
Ho	23	72	86	59	51	25	18	1.44	0.03	36
Er	65	269	344	206	162	75	41	5.44	0.11	80
Tm	10	50	67	36	26	11	5	1.03	0.01	9.4
Yb	68	390	524	279	180	77	32	8.40	0.06	50
Lu	10	65	93	43	26	11	4	1.52	0.00	5.6
Ti	–	–	–	–	–	–	–	–	–	–
Hf	9.90	21.40	28.90	23.20	11.79	13.10	8.39	0.77	–	–
Th	–	–	–	–	–	–	–	–	–	20.01
U	–	–	–	–	–	–	–	–	–	7.77
Th/U	–	–	–	–	–	–	–	–	–	2.41
Yb_N/Gd_N	1.77	8.05	8.96	5.11	3.99	2.04	0.91	6.73	0.40	0.27
Yb_N/Dy_N	0.87	2.29	2.72	1.83	1.32	1.01	0.43	2.30	0.69	0.35
Y_N/Ho_N	0.91	0.92	0.85	0.91	0.91	0.85	1.02	0.84	0.75	0.76
Sm_N/Nd_N	–	–	–	–	–	–	–	–	–	–
Y/Zr	35	192	255	117	118	35	29	12	–	–

Note: All concentration values in ppm.

cf. 120) and distinctly lower in Th/U (0.05) than type (1) zircon (Figs. 7D and 8). Their high HfO_2, U and Yb_N/Gd_N, and low Th/U and Sm_N/Nd_N (=1.33) chemically distinguish the type (3) zones from the type (4) zircon domains described below (Fig. 6B, C).

Type (4), lobate to oscillatory zoned grain tip domains in grain #2 show moderate increases in HfO_2 (1.61–1.98 wt.%) and U (440–550 ppm), and decreases in MREE, Th (16–40 ppm) and Th/U (0.09–0.04) relative to the unmodified prismatic type (1) zircon (grain #2 type (1) zircon: HfO_2=1.74 wt.%; U=129–212 ppm; Th=63–84 ppm; Th/U=0.40–0.50; Fig. 7). Grain #3 does not preserve the unmodified type (1) zircon, but is dominated by type (4) zircon and modified, bright CL zircon similar to type (2). The REE and other trace element features of the type (4) zircon in grain #3 are similar to those in grain #2. Collectively, the type (4) zircon domains in these grains are characterised by lower average Yb_N/Gd_N (=13.8), Gd_N (=20) and Th/U (=0.07) than type (1) zircon, and are distinguished from type (3) domains by their markedly lower Yb_N/Gd_N, which instead is similar to that of type (2) zircon (Fig. 6B). Type (4) zircon in grain #1 (1 analysis, ri15-06-3), characterised in this case by bright CL and dark BSE response, has similar chemical characteristics to the type (3) domains in all respects (e.g. high HfO_2, low Th/U) except for its lower U content (333 ppm) and the lowest measured Yb_N/Gd_N (=3.5). The Ti content is 1.42 ppm, the lowest of any zircon domain analysed.

Type (5) zircon could not be analysed on its own using SIMS as it is fracture-bound and the fractures are much narrower than the diameter of a SIMS beam. However, given its similar BSE and CL response to type (3) and the observation that spot analyses which include such BSE bright fractures

Table 3
Representative electron microprobe data for minerals in RI15

	12/1	12/33	17/44	18/30	16/1	19/1	19/20		15/1	20/7	20/16
	Grt-rim	Grt-trav	Grt-trav	Grt-core	Opx1-trav	Opx2-trav	Opx2-trav		Plag1-trav	Plag2-trav	Plag2-trav
SiO_2	37.01	37.27	37.34	37.59	48.93	49.15	49.12		57.37	57.79	56.85
TiO_2	0.00	0.04	0.04	0.04	0.01	0.01	0.00		0.00	0.00	0.00
Al_2O_3	20.74	20.45	20.70	20.64	0.70	0.70	0.58		26.60	26.56	26.86
Cr_2O_3	0.03	0.00	0.00	0.00	0.01	0.00	0.00		0.00	0.00	0.00
FeO	29.21	29.34	28.75	27.54	35.89	35.23	34.64		0.19	0.17	0.35
MnO	2.54	2.07	1.53	1.27	1.07	1.15	1.18		0.00	0.01	0.03
MgO	2.99	3.18	3.28	2.99	11.45	11.96	12.10		0.00	0.01	0.02
CaO	6.66	7.66	8.08	9.50	0.57	0.72	1.17		8.67	8.17	9.16
Na_2O	0.02	0.01	0.00	0.02	0.01	0.02	0.02		6.71	6.81	6.42
K_2O	0.00	0.00	0.00	0.00	0.00	0.00	0.01		0.42	0.44	0.31
Total	99.20	100.02	99.72	99.60	98.63	98.95	98.81		99.97	99.94	100.00
Num ox	12	12	12	12	6	6	6		8	8	8
Si	2.98	2.98	2.98	3.00	1.99	1.98	1.98		2.58	2.59	2.56
Ti	0.00	0.00	0.00	0.00	0.00	0.00	0.00		0.00	0.00	0.00
Al	1.97	1.93	1.95	1.94	0.03	0.03	0.03		1.41	1.40	1.42
Cr	0.00	0.00	0.00	0.00	0.00	0.00	0.00		0.00	0.00	0.00
Fe	1.97	1.96	1.92	1.84	1.22	1.19	1.17		0.01	0.01	0.01
Mn	0.17	0.14	0.10	0.09	0.04	0.04	0.04		0.00	0.00	0.00
Mg	0.36	0.38	0.39	0.36	0.69	0.72	0.73		0.00	0.00	0.00
Ca	0.57	0.66	0.69	0.81	0.02	0.03	0.05		0.42	0.39	0.44
Na	0.00	0.00	0.00	0.00	0.00	0.00	0.00		0.58	0.59	0.56
K	0.00	0.00	0.00	0.00	0.00	0.00	0.00		0.02	0.03	0.02
Total	8.03	8.05	8.04	8.03	4.00	4.00	4.00		5.02	5.01	5.02
Assuming no Fe^{3+}											
X_{Mg}	0.15	0.16	0.17	0.16	0.36	0.38	0.38				
X_{Alm}	0.64	0.63	0.62	0.59				X_{An}	0.41	0.39	0.43
X_{Pyr}	0.12	0.12	0.13	0.12				X_{Ab}	0.57	0.59	0.55
X_{Sps}	0.06	0.04	0.03	0.03				X_{Or}	0.02	0.02	0.02
X_{Grs}	0.19	0.21	0.22	0.26							
Calculating Fe^{3+}											
Norm-factor	5.05	5.07	5.06	5.03							
Al	1.95	1.90	1.93	1.93							
Cr	0.00	0.00	0.00	0.00							
Fe^{3+}	0.05	0.10	0.07	0.07							
Fe^{2+}	1.90	1.84	1.83	1.75							
Mn	0.17	0.14	0.10	0.09							
Mg	0.35	0.37	0.39	0.35							
Ca	0.57	0.65	0.68	0.81							
Na	0.00	0.00	0.00	0.00							
K	0.00	0.00	0.00	0.00							
Total	5.00	5.00	5.00	5.00							
X_{Mg}	0.16	0.17	0.17	0.17							
X_{Alm}	0.32	0.31	0.30	0.29							
X_{Pyr}	0.12	0.12	0.13	0.12							
X_{Sps}	0.06	0.05	0.03	0.03							
X_{Grs}	0.17	0.17	0.19	0.23							
X_{And}	0.02	0.05	0.04	0.04							

have elevated U but no change in total Zr and Hf, it is considered that the fracture-bound zircon has the same or similar REE compositions and Th/U to type (3).

In summary, type (2) zircon domains retain the high Th/U inherited from type (1) magmatic zircon (>0.5) but show decreases in HfO_2 and in total MREE and HREE so that Yb_N/Hf_N decreases. Types (3) and (4) both have low

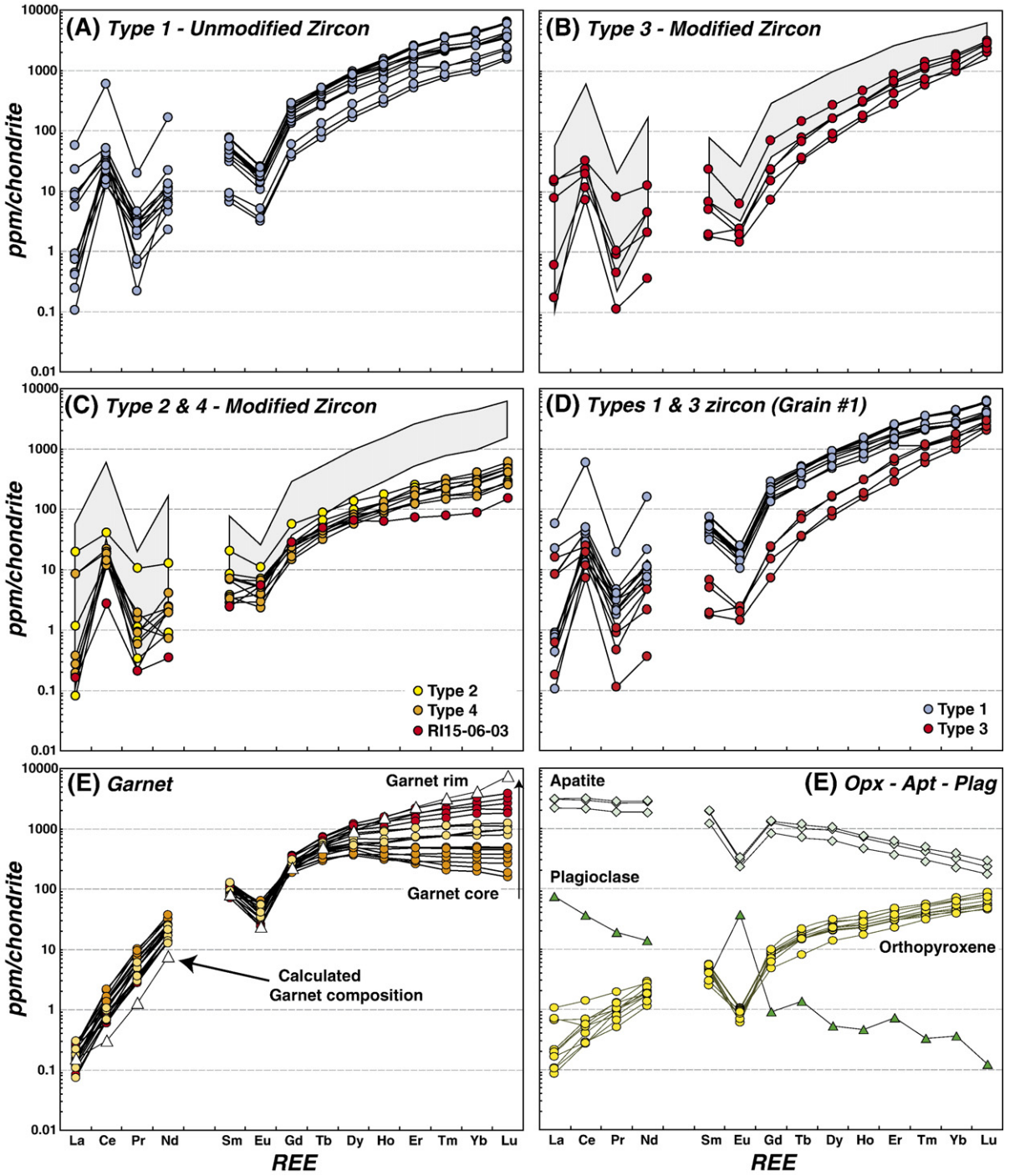

Fig. 6. Chondrite normalised REE (SIMS) data for minerals from RI15, normalised to relative to abundances tabled by Anders and Grevasse (1989). (A) Zircon type (1), grains #1 and #2. (B) Zircon type (3) (grain #1). Shaded field in the background is the range of type (1) zircon from grain #1. (C) Zircon type (2) (modified, but retaining high Th/U) and type (4) (low Th/U). (D) Zircon type (1) contrasted with modified zircon type (3) (grain #1). (E) Garnet. Calculated composition data are presented in Supplementary Data Table 10. (F) Orthopyroxene, apatite and plagioclase.

Th/U (<0.09) but differ in their Th–U–REE characteristics. Type (3) shows marked increases in U and Yb_N/Gd_N, and decreases in the MREE, that are coupled with increasing HfO_2. Type (4) zircon shows marked decreases in Th and all MREE–HREE relative to type (1) zircon, with little increase in U and HfO_2.

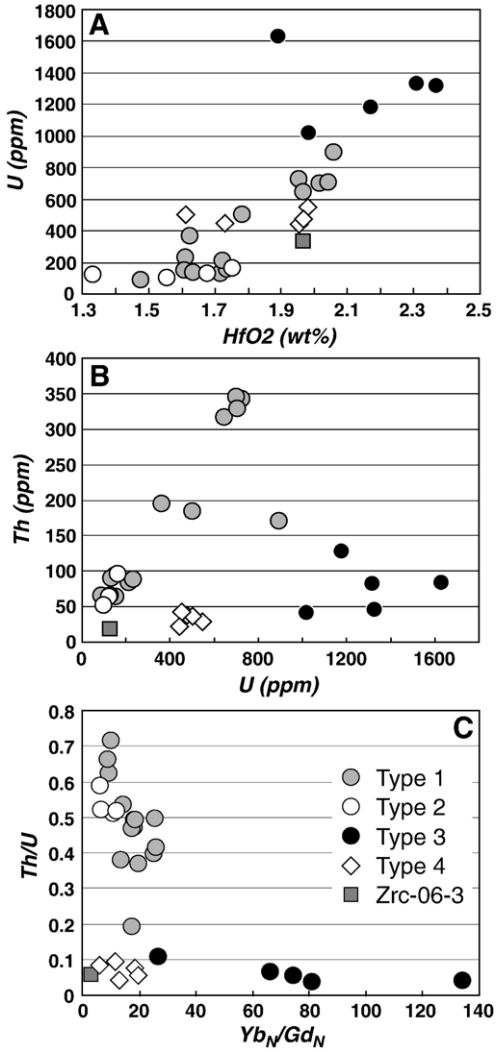

Fig. 7. Compositional covariances in RI15 zircon, classified according to textural types ((1), (2), (3), (4)). (A) U (ppm) versus HfO_2 (wt.%). Type (3) zircons range to the highest U and HfO_2 contents. (B) Th (ppm) vs U (ppm). Types (1) and (2) zircons define a Th–U trend to high Th at high Th/U that is distinct from the marked absolute (type (3) zircon) and relative (type (4) zircon) U enrichments measured in the latter domains. (C) Th/U vs Yb_N/Gd_N. Zircons of types (1), (2) and (4) span similar ranges in Yb_N/Gd_N despite wide variations in Th/U. Only type (3) zircon ranges up to high Yb_N/Gd_N at low Th/U. Unmodified zircon (type (1)) preserves Yb_N/Gd_N that is intermediate between those of modified domains of types 2 and 4 (lower) and type (3) (higher).

5.2.3. Oxygen isotopic compositions: zircon grain #1

Zircon grain #1 has also been analysed by SIMS (Cameca IMS-4f) for its oxygen isotopic composition (Fig. 5B). Analyses were performed at an energy offset of 350 eV following procedures outlined in Valley et al. (1998). Isotope ratios for each spot were referenced against a standard calibration based on interspersed analyses of the Kim-5 zircon standard ($\delta^{18}O = 5.04 \pm 0.07‰$). The six analyses range in $\delta^{18}O$ between 7.2 ± 1.0‰ (1σ) and 4.1 ± 1.0‰ (1σ), with a 3 ± 1.0‰ shift in $\delta^{18}O$ to lighter values correlated with zircon CL/BSE texture. The lighter $\delta^{18}O$ values of between c. 4.1 and 5.4‰ occur in the disturbed zircon micro-domains (3) and (4), or adjacent to a U-enriched fracture (type 5) within the magmatic zircon core.

5.3. Garnet chemistry

5.3.1. Major element zoning

Garnet compositional profiles and element maps are presented in Figs. 8–10 and 3–4, respectively. Line profiles show that garnet ranges from preserved core compositions of $Alm_{59}Prp_{14}Grs_{24}Sps_3$ to rim and near-rim compositions that are relatively enriched in Fe and Mn, and depleted in Ca ($Alm_{67}Prp_{12}Grs_{15}Sps_6$). The length scale over which Ca decreases (from $Grs_{23–24}$ to $Grs_{15–16}$ mol%) and Mn increases (from Sps_3 to Sps_6 mol%) is on the order of 700 to 1200 μm (Fig. 8), so that only garnets with diameters >1–2 mm preserve any of the core composition.

Element maps of garnet grains (Figs. 3 and 4) reveal that the zoning in Mn, Ca and Fe are spatially correlated and to a first approximation concentric with the resorbed

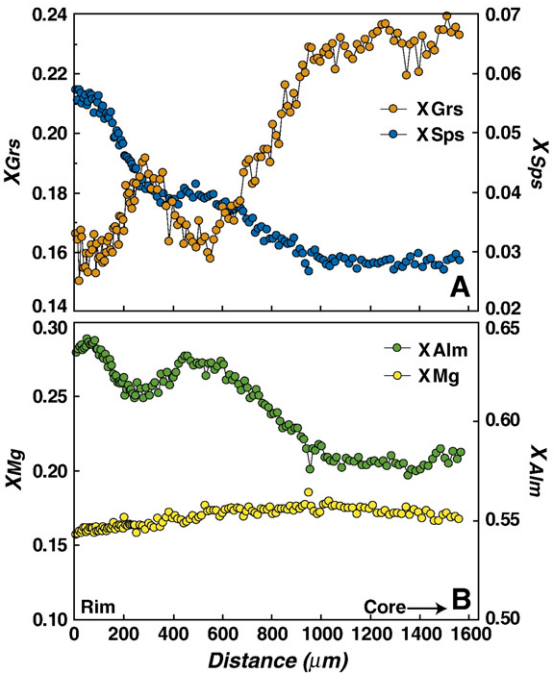

Fig. 8. Major component zoning profiles across RI15 garnet, along the line a–a′ shown on Fig. 4. Note the general rimward decreases in X_{Grs} and X_{Mg} and increases in X_{Sps} and X_{Alm} are disrupted by a small 'hump' in X_{Grs} and 'well' in X_{Sps} and X_{Alm} at 200–500 μm, a relict of less modified garnet within the more broadly modified garnet rim.

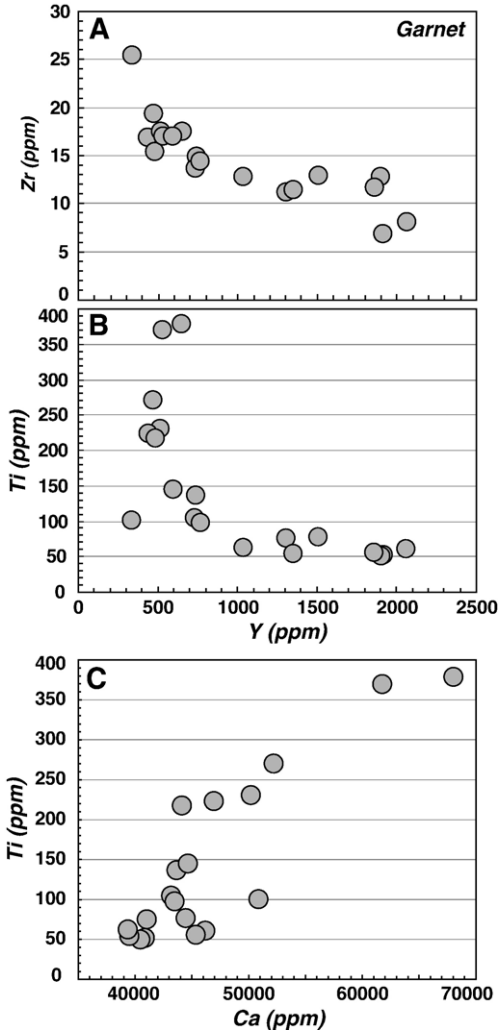

Fig. 9. Trace element variations in garnet: (A) Zr vs Y, (B) Ti vs Y, and (C) Ti vs Ca contents.

edges of the grains (e.g. Fig. 3B). In the largest grains 'kernels' of garnet remain that have core (low Sps, high Grs) compositions, separated by areas with modified compositions (high Sps, lower Grs; Fig. 4). The latter regions are located near and appear to be controlled by magnetite inclusions or by sealed micro-fractures that link between them these inclusions. The localisation of chemical modification of garnet along its resorbed grain edges and in micro-fractures is well illustrated by the element maps for Y (Figs. 3D and 4D). These show significant relative enrichments in Y only within 100 μm of the grain edges adjacent to plagioclase and within sealed micro-fractures. The enrichments in Y correlate with Mn zoning but are much more spatially restricted. These relationships are explored further using SIMS trace element analyses below.

5.3.2. Trace element chemistry and zoning features

REE patterns for garnets from RI15 are presented in Fig. 6E. These display a consistent core to rim increase

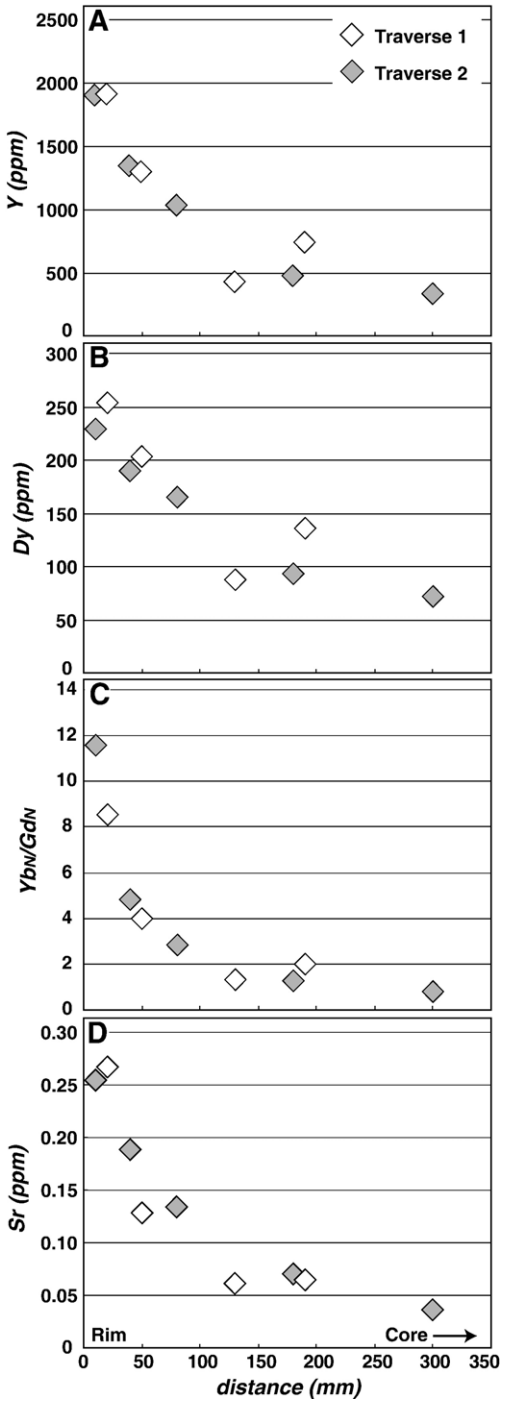

Fig. 10. Trace element variations across the outer, near-rim, region of the garnet shown in Fig. 4A. Distance is plotted as location of the SIMS spot from the present edge of the garnet so that two SIMS traverses (1 and 2, Fig. 9A) can be presented on the same diagrams.

in HREE relative to LREE, with HREE forming a fanning array ranging from $Yb_N = 200$ to $Yb_N = 4000$. All garnet is characterised by negative Eu anomalies that are deeper in rims than cores (Eu/Eu* = 0.32 cores; = 0.16 rims).

Garnet core regions located >200 μm interior to grain boundaries and >100 μm from visible magnetite inclusions are typified by gently sloping and flat to slightly 'depleted' HREE patterns ($Yb_N/Gd_N = 3.1–0.8$; $Gd_N = 120–260$) with a slight REE 'hump' centred on Dy ($Yb_N/Dy_N = 0.3–1$). Such REE cores or 'kernels' constitute some 75–85% of the garnet volume. Core Y is 500–700 ppm, Zr 25–13 ppm, and Ti 400–100 ppm in these areas (Fig. 9).

Garnet zones to steeper HREE ($Yb_N/Gd_N = 4–12$; $Gd_N = 300$), higher Y (2200 ppm), lower Zr (13–7 ppm), and lower Ti (50 ppm) rimwards (Figs. 9 and 10). Two SIMS traverses of garnet inwards from grain edges adjacent to coronal plagioclase and orthopyroxene demonstrate that this zoning occurs within 100–120 μm of the resorbed rim (Fig. 10). Rimward increases in Y and Dy are strongly correlated with increases in Yb_N/Gd_N, and with decreases in Zr and Ti. Even Sr, present in very low abundances in garnet (0.05 ppm in cores) shows a five-fold increase within 100 μm of resorbed garnet edges adjacent to coronal plagioclase (Fig. 10D). This feature is consistent with the Y maps (Figs. 3D and 4D). The trace element zoning profiles are coincident with, but occur over a much narrower width than, the major element zoning profiles characterised by core-to-rim increases in Sps and decreases in Grs. The marked near-rim increases in Y and HREE associated with resorbed rims are not observed where garnet is still in contact with quartz.

The evidence from the REE and major zoning profiles, in particular the spatial control exerted by the resorbed garnet grain interface with plagioclase, are consistent with the interpretation that the HREE were preferentially held back in the garnet as it was broken down during the granulite facies reaction that produced the orthopyroxene + plagioclase coronas. The garnet was modified in its REE to high rim HREE concentrations during its consumption rather than during growth. This interpretation will be tested using garnet–orthopyroxene REE distribution relationships.

5.4. Orthopyroxene REE Chemistry

Orthopyroxene ($X_{Mg} = 36.3$; $Al_2O_3 = 0.83$ wt.%) formed with plagioclase on garnet is homogeneous in REE. Patterns are characterised by elevated HREE ($Yb_N/Gd_N = 6.5$ at $Dy_N = 23$) and strong negative Eu anomalies (Eu/Eu* = 0.14; Fig. 6F). The orthopyroxene contains 2–4 ppm Zr, 34 ppm Y and 131 ppm Ti.

5.5. Trace element chemistry of other phases

Apatite in RI15 is characterised by high REE ($Gd_N = 1000$), $Ce_N/Yb_N = 9.4$, and a strong negative Eu anomaly (Eu/Eu* = 0.19) (Fig. 6F). *Plagioclase* in RI15 has a fractionated LREE/HREE pattern ($Ce_N/Yb_N = 100$) with very low HREE (<1) and a strong positive Eu anomaly (Eu/Eu* = 17.2). As this plagioclase was analysed along with orthopyroxene that has a much lower LREE content (Fig. 6F) in the same SIMS session, its high measured LREE is real and not an analytical artifact. SIMS analysis of *magnetite* indicates that it has <1 ppm Zr.

6. REE distributions between zircon, garnet and orthopyroxene

The REE and other trace element data described above and presented in Tables 1 and 2 can be used to calculate apparent trace element distribution coefficients ($D_{element}$) that can be compared with empirical or experimentally derived D values inferred to represent equilibrium (e.g. Hinton and Upton, 1991; van Westrenen et al., 1999; Harley et al., 2001; Rubatto et al., 2001; Rubatto, 2002; Whitehouse and Platt, 2003; Kelly and Harley, 2005). In principle this is straightforward, but in practice such comparisons are hampered by a relative paucity of experimental data for the mineral pairs and compositions of interest at appropriate crustal P–T conditions, and by limitations on the extrapolation of trace element distribution models to those P–T–X conditions (van Westrenen et al., 1999).

In this study we adopt the approach of comparing apparent REE distribution coefficient patterns calculated from the zircon, garnet and orthopyroxene REE data, with empirical D values and patterns determined from crustal granulites that on textural and other mineralogical criteria are considered to represent equilibrium. These comparisons are used to establish whether equilibrium has been approached or attained between zircon and the high-grade metamorphic assemblages now present in RI15, and hence to evaluate the link between zircon age, chemistry and metamorphism in this case.

6.1. Orthopyroxene–garnet REE relationships

Before proceeding to evaluate the REE systematics between zircon and garnet and the event significance of

zircon ages in RI15, it is useful to consider the distribution of the REE between garnet and orthopyroxene, the Fe–Mg minerals indicative of granulite facies metamorphism and *P–T* evolution in RI15.

D_{REE}(opx/grt) calculated for orthopyroxene–garnet pairs based on the preserved core compositions of garnet (Fig. 11; Table 4) are, as expected from the reaction texture in RI15, far removed from equilibrium when compared with empirical D_{REE}(opx/grt) values obtained from texturally equilibrated garnet–orthopyroxene pairs in other granulite facies rocks (Harley et al., 2001; Harley, unpubl. data). The latter indicate that equilibrium D_{REE}(opx/grt) lie in the range 0.03–0.01 for the HREE. In the case of RI15, the HREE contents of the coronal orthopyroxenes are too high in comparison with those of the garnet cores so that, for example, D_{Yb}(opx/grt) is near 0.2, an order of magnitude greater than preferred equilibrium values (0.01–0.02: Harley et al., 2001; Harley, unpubl. data).

In contrast, D_{REE}(opx/grt) calculated based on the narrow, HREE-enriched garnet rim compositions closely approach likely equilibrium values (e.g. D_{Gd}=0.025 cf 0.03; D_{Yb}=0.021 cf. 0.012; Fig. 11). This is consistent with the textural and zoning evidence cited above that garnet was modified in its HREE content during its reaction, under granulite facies conditions, to produce the orthopyroxene–plagioclase coronas. The model garnet REE rim composition that would be in equilibrium with coronal orthopyroxene can be estimated assuming that the empirical D_{REE} values from other granulite assemblages (Harley et al., 2001; Harley, unpubl. data) represent equilibrium. This calculated garnet composition, depicted in Fig. 6E, is consistent with the pattern of REE change seen in the garnet analysis population as a whole, and with the near-rim zoning profile established from our SIMS analyses

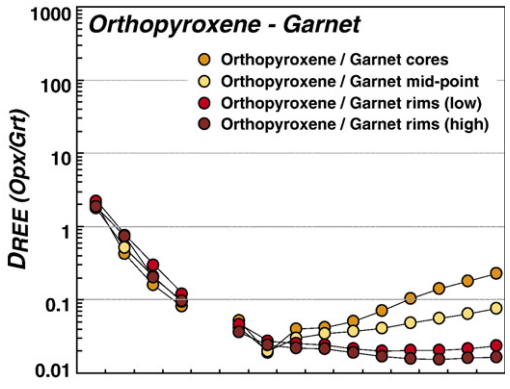

Fig. 11. REE distribution patterns between orthopyroxene and garnet in RI15.

(Fig. 10). Estimated 'on rim' Yb_N/Gd_N of 15–16 at Gd_N=260, and Yb_N=4100 (Yb=666 ppm) obtained by extrapolating our garnet trace element composition profiles (Fig. 10) to the resorbed grain edges match the calculated garnet HREE very well.

6.2. Zircon–garnet REE relationships

The equilibrium distribution of REE between zircon and Ca-poor Fe–Mg garnet (X_{Mg}=0.45–0.65) at temperatures of 900–1100 °C has previously been empirically defined using the compositions of unzoned zircons and inclusion-free garnets in garnet–mesoperthite–quartz leucosomes from the Napier Complex (Harley et al., 2001; Kelly and Harley, 2005). These yield calculated $D_{MREE–HREE}$(zrc/grt) similar to those obtained by Whitehouse and Platt (2003) for a garnet-bearing pelite from the Betic Cordillera. Based on this, REE distributions that represent zircon–garnet equilibrium under high temperature metamorphic conditions are likely to have D_{REE}(zrc/grt) values of D_{Gd}=0.9, D_{Ho}=0.8 and D_{Yb}=0.6–0.7 (Harley et al., 2001).

Unmodified 2840 Ma type (1) zircon is, as expected from its textural and magmatic chemical zoning features, well out of equilibrium with any chosen garnet core REE composition. Apparent D_{REE}(zrc/grt) for the MREE–HREE based on type (1) zircon coupled with garnet cores range over an order of magnitude, from D_{Gd}=0.8 to D_{Yb}=8 (Fig. 12A, B). The apparent $D_{MREE–HREE}$(zrc/grt) calculated for zircon type (1) in combination with resorbed garnet rims are closer to unity (D_{Gd}=0.5 to D_{Yb}=1; Fig. 12C), and to the equilibrium values suggested above (Harley et al., 2001; Whitehouse and Platt, 2003). However, this distribution cannot represent zircon–garnet equilibrium as the reaction texture associated with formation of the high-HREE garnet rims is texturally post-magmatic.

D_{REE}(zrc/grt) calculated for combinations of texturally and chemically modified zircon micro-domains (low Th/U types (3) and (4), and high Th/U type (2)) with garnet cores and rim compositions are presented in Fig. 12. The apparent D_{REE} calculated using the both the lowest REE garnet cores and cores modified to relatively flat HREE are strongly fractionated. Types (2) and (4) zircon, with their lowered HREE contents, yield D_{Gd} near 0.1–0.2 and D_{Yb} in the range 0.35–1. Type (3) zircon, which show preferential MREE depletion relative to type (1), yields D_{REE}(zrc/grt) that range from 0.1 (D_{Gd}) to 1.5–5 (D_{Yb}). In short, no combination of modified zircon with core garnet compositions yield D_{REE}(zrc/grt) that are comparable across the range of MREE and HREE to those reported

Table 4
Calculated mineral/mineral and mineral/rock REE distribution coefficients

	Orthopyroxene/garnet (Fig. 11)				Zircon/rock (Fig. 13C)				
	Grt cores	Grt midpoint	Grt rims (low)	Grt rims (high)	Hinton and Upton (1991)	Type (1) zrc /SLC (Comp 1)	Type (1) zrc /SLC (Comp 2)	Type (1) zrc /SLC (Comp 3)	Type (1) zrc /SLC (Comp 4)
La	2.04	1.79	2.20	1.88	0.01	0.08	0.01	0.01	0.01
Ce	0.43	0.51	0.75	0.74	0.02	0.57	0.38	0.54	0.34
Pr	0.16	0.21	0.30	0.20	0.06	0.06	0.04	0.05	0.04
Nd	0.08	0.09	0.12	0.10	0.18	0.27	0.15	0.21	0.13
Sm	0.05	0.04	0.05	0.04	1.1	1.8	1.7	1.3	1.5
Eu	0.02	0.02	0.03	0.02	2.3	0.5	0.5	0.4	0.5
Gd	0.04	0.03	0.03	0.02	5.0	8.6	8.3	6.4	7.3
Tb	0.04	0.03	0.02	0.02	11				
Dy	0.05	0.04	0.02	0.02	24	38	37	30	32
Ho	0.07	0.04	0.02	0.02	49	70	69	58	60
Er	0.10	0.05	0.02	0.02	94	133	131	118	115
Tm	0.14	0.06	0.02	0.02	171				
Yb	0.18	0.06	0.02	0.02	293	233	231	225	202
Lu	0.23	0.08	0.02	0.02	472	297	292	313	259

	Low-HREE core garnet (Fig. 12)				Normal core garnet (Fig. 12)			
	Type (1) zrc/grt	Type (2) zrc/grt	Type (3) zrc/grt	Type (4) zrc/grt	Type (1) zrc/grt	Type (2) zrc/grt	Type (3) zrc/grt	Type (4) zrc/grt
La	2.75	30.13	35.27	20.84	2.42	26.45	30.97	18.30
Ce	15.20	16.27	11.85	12.88	18.18	19.46	14.17	15.41
Pr	0.27	0.48	0.10	0.18	0.35	0.62	0.12	0.23
Nd	0.22	0.17	0.12	0.10	0.25	0.20	0.14	0.11
Sm	0.46	0.12	0.05	0.06	0.37	0.09	0.04	0.04
Eu	0.31	0.16	0.04	0.09	0.32	0.16	0.05	0.09
Gd	0.80	0.17	0.08	0.10	0.61	0.13	0.07	0.08
Tb	0.85	0.17	0.14	0.11	0.70	0.14	0.12	0.09
Dy	1.30	0.21	0.27	0.16	0.95	0.16	0.20	0.12
Ho	2.49	0.36	0.65	0.28	1.43	0.21	0.37	0.16
Er	4.61	0.60	1.51	0.48	2.13	0.28	0.70	0.22
Tm	6.74	0.73	2.92	0.71	2.71	0.29	1.17	0.29
Yb	8.63	0.96	4.67	0.91	3.08	0.34	1.67	0.33
Lu	13.18	1.51	9.16	1.45	4.34	0.50	3.02	0.48

	Rim garnet (Fig. 12)				Model rim garnet (Fig. 12)			
	Type (1) zrc/grt	Type (2) zrc/grt	Type (3) zrc/grt	Type (4) zrc/grt	Type (1) zrc/grt	Type (2) zrc/grt	Type (3) zrc/grt	Type (4) zrc/grt
La	2.96	32.45	37.99	22.45	6.73	73.69	86.27	50.97
Ce	26.65	28.52	20.77	22.59	70.85	75.84	55.24	60.06
Pr	0.51	0.90	0.18	0.34	1.28	2.26	0.46	0.85
Nd	0.32	0.25	0.18	0.14	0.67	0.53	0.38	0.30
Sm	0.40	0.10	0.04	0.05	0.48	0.12	0.05	0.06
Eu	0.44	0.22	0.06	0.13	0.60	0.31	0.09	0.18
Gd	0.52	0.11	0.05	0.06	0.60	0.13	0.06	0.08
Tb	0.49	0.10	0.08	0.06	0.49	0.10	0.08	0.06
Dy	0.55	0.09	0.12	0.07	0.49	0.08	0.10	0.06
Ho	0.70	0.10	0.18	0.08	0.60	0.09	0.16	0.07
Er	0.89	0.12	0.29	0.09	0.66	0.09	0.22	0.07
Tm	0.99	0.11	0.43	0.11	0.66	0.07	0.29	0.07
Yb	1.04	0.12	0.56	0.11	0.61	0.07	0.33	0.06
Lu	1.35	0.15	0.94	0.15	0.70	0.08	0.48	0.08

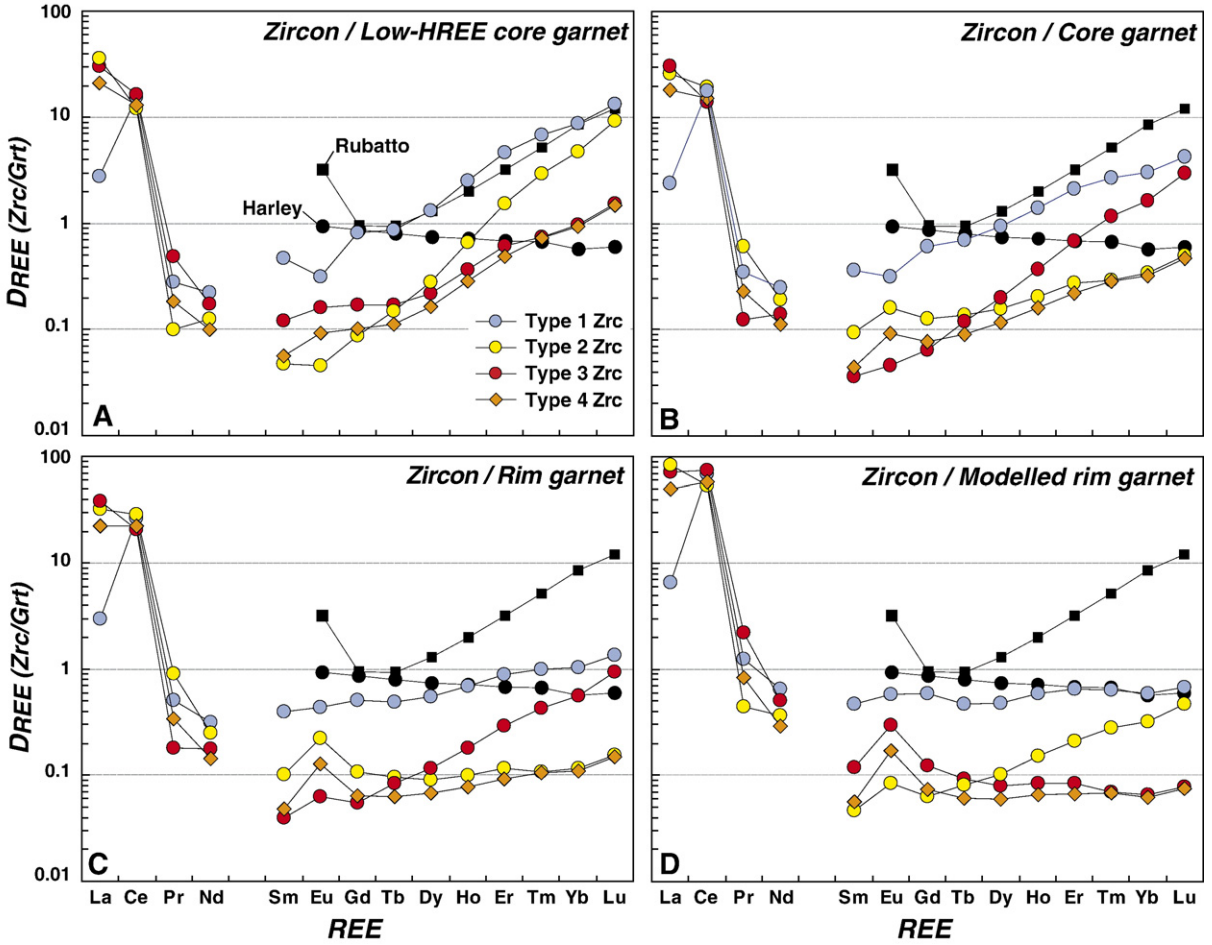

Fig. 12. REE distribution patterns of garnet in RI15, paired with averaged REE compositions of types (1), (2), (3) and (4) zircon. The equilibrium D_{REE}(Zrc/Grt) values of Harley et al. (2001) and Rubatto (2002) are presented for comparison. (A) D_{REE}(Zrc/Grt) calculated using the compositions of low-HREE garnet cores. (B) D_{REE}(Zrc/Grt) calculated using the average compositions of garnet cores. (C) D_{REE}(Zrc/Grt) calculated using the compositions of high-HREE garnet rims. (D) D_{REE}(Zrc/Grt) calculated using the calculated composition of a high-HREE garnet rim predicted from orthopyroxene–garnet equilibrium and consistent with extrapolation of the REE zoning profiles (Fig. 11) to the outermost garnet rim.

by Harley et al. (2001) and Whitehouse and Platt (2003). In all cases, because the MREE in modified zircon is relatively low the resultant D_{REE}(zrc/grt) are also much lower than the values preferred by Rubatto (2002) as equilibrium D_{REE}.

D_{REE}(zrc/grt) calculated using the resorbed high-HREE garnet rims coupled with modified zircon micro-domains types (2) and (4) are similar across the range of MREE–HREE, but uniformly lower by an order of magnitude (D_{Gd}=0.065–0.105, D_{Yb}=0.105) than probable equilibrium values (Harley et al., 2001; Whitehouse and Platt, 2003). Garnet rims coupled with type (3) zircon, the dominant modified micro-domain type, yield fractionated D_{REE}(zrc/grt) that vary from 0.06 at Gd to near unity at Lu. Similar relationships hold if the modelled high-HREE garnet rim calculated from D_{REE} (opx/grt) is used to derive apparent D_{REE}(zrc/grt) for modified zircon coupled with garnet close to REE equilibrium with orthopyroxene and plagioclase: all such D_{REE}(zrc/grt) are lower, by up to an order of magnitude, than the equilibrium values suggested in current literature (Fig. 12D).

The very low D_{REE}(zrc/grt), especially for the MREE (Sm, Eu, Gd, Tb, Dy) result because zircon and garnet MREE, and to a lesser extent HREE, change in opposite directions during the textural modifications to the minerals. This behaviour would not be expected if the two minerals were changing in composition simultaneously to achieve or approach equilibrium, for any currently accepted or proposed D_{REE}(zrc/grt). Given equilibrium D_{REE}(zrc/grt) values near unity (Harley et al., 2001; Whitehouse and Platt, 2003) or greater than

unity (Rubatto, 2002), any zircon either forming or undergoing chemical modification as garnet zones to higher MREE–HREE during its reaction would be expected to show relative *increases* in its MREE. Instead, in this example the changes in REE in zircon are in the opposite sense and so must be decoupled from the REE zoning observed in garnet. Chemical modification of zircon in this case cannot be associated with or ascribed to the consumption of garnet, and so cannot be ascribed to the granulite facies *P–T* conditions associated with formation of this texture and resultant orthopyroxene+plagioclase bearing mineral assemblage.

7. Mineral–whole rock REE and trace element relationships

7.1. Mineral REE and the calculated REE composition of RI15

The REE composition of RI15 has been calculated from mass balance, using the observed modal proportions of the REE-bearing minerals estimated by point-counting BSE images, and their REE contents (Supplementary Table 8). The calculations have been carried out in two stages because of the reaction of initial garnet to produce plagioclase and orthopyroxene. First, the modal proportions of plagioclase and orthopyroxene in the corona textures have been estimated by point counting and an average corona REE composition calculated. This has then been weighted according to its total area proportion, corrected for density, and added to the weighted proportions of remaining 'core' garnet, garnet rims, apatite and zircon to arrive at a bulk rock REE pattern. Two REE patterns calculated using different proportions of garnet, coronas and apatite are presented in Fig. 13. These are relatively robust to variation in the estimates of accessory zircon because of the high modal proportion of garnet, but are sensitive at the LREE end to the apatite:garnet ratio. Nevertheless, the calculated bulk rock REE are characterised by $LREE_N$ near 150–200, a strong negative Eu anomaly (Eu/Eu*=0.29), and $HREE_N$ at 200–300. These estimates are consistent with XRF data obtained independently on La, Ce, Nd and Y (Snape, 1997) (Fig. 13).

The estimated bulk rock REE pattern for RI15 depicted in Fig. 13 is far removed from any likely melt composition, as all REE are high and HREE<LREE. Based on this and its major element composition (Supplementary Data Table 8) RI15 is interpreted to originally have been a site of crystal accumulation in the SLC, rather than a fractionated late stage liquid. This is supported by our calculations (see below) that show the distribution of REE between magmatic zircon type (1) and the bulk rock (RI15) do not follow equilibrium zircon–liquid relationships as estimated by Hinton and Upton (1991).

7.2. SLC estimated melt composition and the magmatic character of zircon type (1)

Based on an extensive geochemical study of the Scherbinina Layered Complex, Snape (1997) was able to identify a main sequence of meta-igneous protoliths, varying in composition from ferro-diorite to gabbro that preserved internally consistent geochemical trends and isotopic features. Complete REE data were obtained on 8 main sequence rocks that span a range in Mg-number from 28 to 64 and also have high Sr (Supplementary Data Table 9). These REE data are shown as chondrite normalised plots in Fig. 13B along with an averaged REE pattern for the SLC. This average was calculated taking into account the relative proportions of the major rock types within the main sequence and excluding the lowest REE rocks, which from Mg/Fe and SiO_2 is likely to be a cumulate.

This average SLC REE pattern has been combined with averaged zircon type (1) REE compositions to derive apparent zircon/melt distribution coefficients D_{REE}(zrc/rock) in Fig. 13C. These are in excellent agreement with D_{REE}(zrc/melt) values previously produced by Hinton and Upton (1991) for all REE apart from Ce and Eu, being only slightly lower at Yb and Lu and higher at La. The departure at Ce is explained by the magnetite-bearing SLC containing zircon that has appreciable Ce^{4+}, as the D_{Ce} (zrc/melt) value tabled in Hinton and Upton (1991) is for Ce^{3+} interpolated from La and Pr contents. The deviation at Eu is explicable by the early, near liquidus crystallisation of feldspar in the SLC (Snape, 1997) prior to zirconium saturation and consequent zircon crystallisation. The other D_{REE}(zrc/rock) data support the contention that zircon type (1) is magmatic in origin, crystallised from melts with compositions represented now by the main SLC ferro-diorite/ferro-gabbro rock suite rather than from a composition like that of RI15 itself, which as shown above from mass balance considerations is far removed in terms of its REE and major elements from viable melt compositions in the SLC.

7.3. SLC average melt composition compared with garnet core REE patterns

It has already been argued and demonstrated on the basis of textures and inter-mineral REE relationships

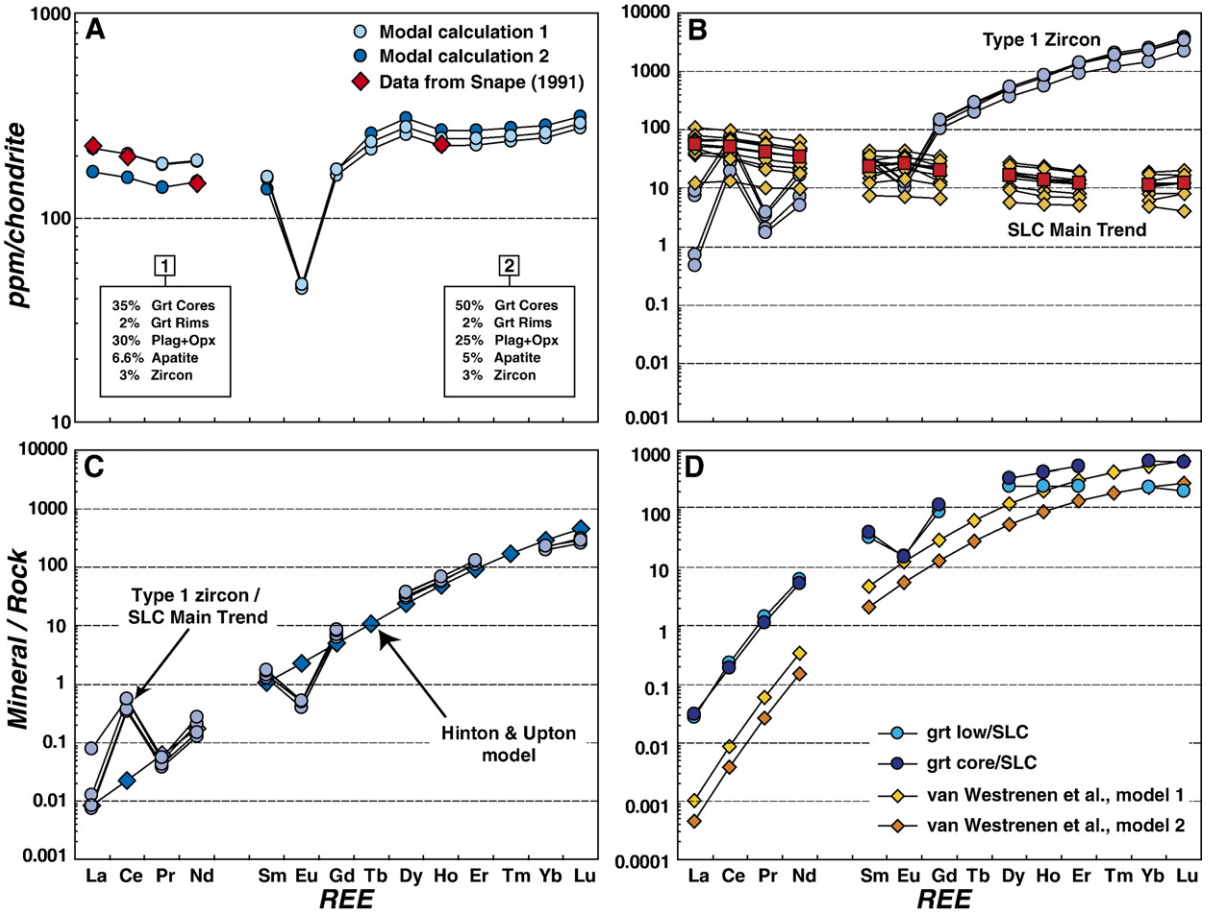

Fig. 13. (A) Chondrite normalised whole rock REE data plot showing two REE patterns for RI15 calculated from the mineral REE data and mass balance relationships (the mass proportions of each phase as given on the diagram). (B) Chondrite normalised whole rock REE data patterns for all SLC 'main sequence' rocks analysed by Snape (1997), plotted against typical type (1) zircon REE compositions. The averaged SLC REE pattern (squares) is based on a weighted mean of these rocks that produces a bulk rock composition with SiO_2=50 wt.% and Mg#=51. This average is used in the calculation of D_{REE}(zrc/melt) in C. (C) Comparison of D_{REE}(zrc/melt) calculated using averages of the compositions of type (1) zircon and the average SLC bulk composition (Fig. 13A) with D_{REE}(zrc/melt) as determined by Hinton and Upton (1991). (D) REE diagram showing D_{REE}(grt/rock) produced by combining low-HREE garnet core and average garnet core compositions with the average REE composition of the SLC (circles). These are compared with D_{REE}(grt/melt) calculated using the model of van Westrenen et al. (1999) at 8 kb and 900 °C and tuned so that D_{REE}(grt/melt) and D_{REE}(grt/rock) overlap for the HREE at and beyond Er (diamonds).

that initial metamorphic garnet in RI15 did not form in equilibrium with magmatic zircon type (1). An additional test of this interpretation can be made using modelled garnet–melt distribution coefficients. In principle the REE composition of garnet that would be in equilibrium with a melt with the average SLC composition, and hence with magmatic zircon type (1), can be calculated using the D_{REE}(grt/melt) model of van Westrenen et al. (1999). However, in application this approach is highly model-dependent. As an alternative, we have compared the D_{REE}(grt/rock) produced by coupling the low-HREE and average core garnets in RI15 with the average SLC composition, with model D_{REE}(grt/melt) values fitted across the whole range of REE but calculated after adjusting model parameters (e.g. D_{Mg}) to at least produce a match between the observed and calculated HREE beyond Er.

The results of this type of comparison are presented in Fig. 13D and Table 5. Given their HREE contents, the garnets in RI15 are far too rich in MREE and LREE to be in equilibrium with the SLC average rock composition, if extrapolation of the van Westrenen et al. (1999) model is realistic for these rocks. Given that the SLC average main sequence composition conforms to zircon-melt equilibrium calculations, these results confirm the interpretation from textures and mineral chemistry that the initial garnets in RI15 are either too low in HREE or

Table 5
Calculated garnet/rock REE distribution coefficients for SLC compositions

	Garnet/rock (Fig. 13D)			
	Grt low/SLC	Grt core/SLC	Model prediction 1	Model prediction 2
La	0.00	0.00	0.00	0.00
Ce	0.02	0.02	0.00	0.00
Pr	0.14	0.11	0.01	0.00
Nd	0.62	0.54	0.03	0.02
Sm	3.25	4.07	0.48	0.21
Eu	1.61	1.55	1.26	0.55
Gd	9.17	11.93	2.97	1.30
Tb	–	–	6.34	2.78
Dy	24.96	34.02	12.26	5.38
Ho	24.37	42.58	20.69	9.08
Er	25.04	54.16	31.15	13.67
Tm	–	–	42.67	18.73
Yb	23.74	66.50	54.10	23.74
Lu	20.41	61.97	64.44	28.28

too high in MREE to be in equilibrium with SLC melt and hence magmatic zircon type (1).

8. Discussion

8.1. REE and the link between zircon modification, U–Pb age and metamorphic history

As inferred by Harley et al. (1998), 2840 Ma type (1) zircon in the SLC is demonstrably of magmatic origin. This is supported by its morphology and internal texture, its trace element zoning patterns and by the very good agreement between D_{REE}(zrc/rock) calculated using zircon type (1) and the average REE composition of the SLC, with the D_{REE}(zrc/melt) values of Hinton and Upton (1991). As is evident from textural relationships, garnet in RI15 did not grow in equilibrium with this early zircon (zircon type (1)), and the core garnet composition is too elevated in MREE or low in HREE to be in equilibrium with any reasonable estimate of the SLC model melt composition.

Chemical and textural modification of zircon to produce the varied REE and Th/U types (2), (3) and (4) is considered, based on the consistency in the U–Pb data that records one significant episode of Pb loss coincident with new zircon formation, to have occurred at c. 510 Ma. However, the possibility of earlier modification and Pb-loss (e.g. within 100 Ma of the magmatic age of 2840 Ma) cannot be excluded using this data alone, as subsequent extensive Pb loss at 510 Ma would obscure any early partial Pb loss pattern. Examination of the discordant U–Pb zircon data for RI43 and RI15 (Fig. 2) shows that three grains lie off and to the younger side of the principal discordia, possibly reflecting c. 510 Ma Pb loss from zircon previously reset at 2600–2700 Ma.

The U–Pb data taken in isolation could be used to infer that zircon underwent modification, and Pb-loss, in the metamorphic events that produced the initial garnet–quartz–magnetite–(orthopyroxene) granulite facies assemblage and the overprinting, texturally mature, orthopyroxene–plagioclase coronas that surround resorbed garnet. However, D_{REE}(zrc/grt) calculated for all modified zircon types coupled with core metamorphic garnet are inconsistent with the chemical modifications in zircon occurring in response to garnet formation. The apparent D_{REE}(zrc/grt) are too low, especially for the MREE Sm, Eu, Gd, Tb and Dy, in comparison to even the lowest current estimates for equilibrium zrc/grt REE distributions under granulite facies conditions (0.9–0.8: Harley et al., 2001; Whitehouse and Platt, 2003). Moreover, rather than the magmatic zircon type (1) increasing in MREE and decreasing in HREE to approach equilibrium with newly-formed garnet, the zircon modifications all involve extensive decreases in MREE. The simplest interpretation of the zircon REE data is that the original magmatic zircon was chemically unresponsive to the event that formed the ubiquitous garnet in RI15, as illustrated in the schematic textural evolution diagram of Fig. 14.

These REE-based arguments are also relevant to the issue of whether zircon modification occurred during the reaction of garnet to produce orthopyroxene–plagioclase coronas. As noted in a previous section, the D_{REE}(opx/grt) calculated for coronal orthopyroxene and high-HREE garnet rims approach those inferred to represent equilibrium in other granulite facies rocks, suggesting that the outermost edges of resorbed garnet grains are in local REE equilibrium in the garnet–orthopyroxene–plagioclase–quartz granulite facies assemblage that was produced at $P \approx 8$ kbar and $T \approx 800$ °C. The D_{REE}(zrc/grt) calculated for all *modified* zircon types coupled with the high-HREE resorbed garnet rim compositions are inconsistent with the chemical/textural modifications in zircon occurring in concert with the HREE increases in garnet. This further implies that the zircon chemical modification did not occur in response to the development of the orthopyroxene–plagioclase reaction texture and the sub-millimetre scale redistribution of REE involved in its formation (Fig. 14). The apparent D_{REE}(zrc/grt) are too low, by up to an order of magnitude, for the MREE and most HREE in comparison with equilibrium zrc/grt REE distributions (Harley et al., 2001; Whitehouse and

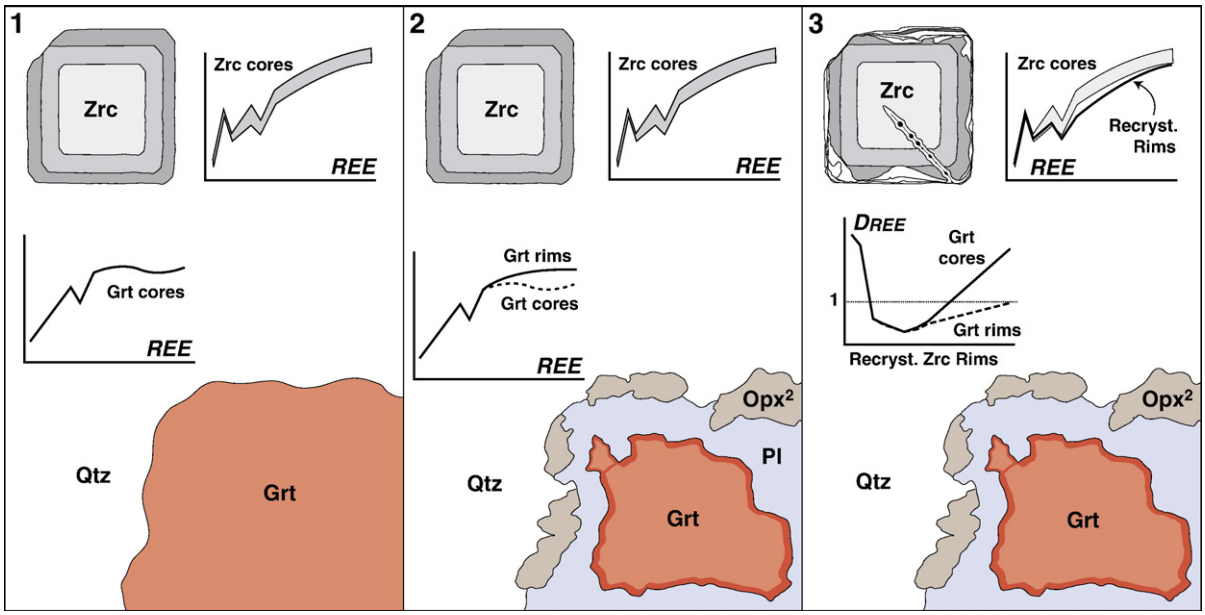

Fig. 14. Schematic diagram showing the proposed evolution of REE signatures and textures in zircon and garnet in RI15, starting from the growth of initial garnet in RI15 (stage 1, high-*P* granulite facies) and terminating with the fluid-activated modification of pre-stage 1 magmatic zircon (stage 3, 510 Ma).

Platt, 2003). Even though garnet shows an order of magnitude increase in its HREE over a length scale of c. 100 μm, similar increases in REE are not observed on the rims of zircon, even where the zircon is adjacent to former garnet grain boundaries that have clearly been replaced by orthopyroxene and plagioclase. This lack of HREE enhancement in zircon, which as noted previously would be expected to occur if it was undergoing chemical modification to approach equilibrium with reactant garnet, demonstrates that the original magmatic zircon in RI15 also was unresponsive to the granulite facies event associated with production of the garnet–orthopyroxene–plagioclase–quartz assemblage, as shown schematically in Fig. 14.

8.2. Modification of zircon at 510 Ma: the role of fluid

The zircon–garnet REE data and textural relationships indicate that the ancient magmatic zircons modified their REE in response to a late event, at c. 510 Ma, that post-dates the high grade metamorphic event(s) recorded in RI15, rather than occurring prior to granulite metamorphism. The key observations in this respect are that the grain shapes of zircon in RI15 are locally modified to subhedral morphologies adjacent to orthopyroxene that has formed after garnet, and that the chemically modified domains (e.g. type (3), grain #1, Fig. 5) are often concentric with these modified grain shapes, or are localised along sealed fractures that are seated in these modified, post-orthopyroxene grain edges. Micro-fracturing has produced fluid inclusion arrays that can be traced in thin section across zircon grains with differing orientations, with plagioclase and orthopyroxene intervening between the zircons. Zircon along these micro-fractures is characterised by bright BSE and dark CL responses, associated with enhanced U contents, and so bear the chemical hallmarks of type (3) zircon as described previously.

These features strongly indicate zircon modification through an inward (into-grain) movement of surface-parallel but fracture-controlled planar to lobate chemical fronts, consistent with fluid-mediated infiltration and chromatographic exchange and probably accompanied by in-situ dissolution–reprecipitation (e.g. McLaren et al., 1994; Hartmann et al., 1997; Hoskin and Black, 2000; Carson et al., 2002). The 3±1.0‰ shift in zircon $\delta^{18}O$ to lighter values correlated with textural modification in zircon grain #1 supports the interpretation that fluid infiltration stimulated the extensive Pb-loss from zircon at c. 510 Ma and led to its localised chemical modification to produce zircon types (2), (3), (4) and (5).

This c. 510 Ma fluid-infiltration event recorded by the zircons in RI15 may be related to the amphibolite to greenschist facies emplacement of granitic pegmatites into the Rauer Terrane gneisses late in the Prydz Tectonic Event. Kinny et al. (1993) have constrained the emplacement of one such pegmatite to 500±12 Ma, identical within error to the age of the isotopically reset

concordant zircons from the SLC. The SLC itself is dissected by 10 cm–1 m width planar granitic pegmatites with lateral separations of 10 to 40 m (Harley et al., 1998), which are associated with small-scale dextral shear zones. Carson et al. (2002), in a study of the behaviour of zircon in gneisses retrogressed by the emplacement of a pegmatite under amphibolite facies conditions in the Napier Complex, demonstrated from ion microprobe depth profiling that fluid infiltration into zircon via microfracture networks is an effective means of causing localised U–Pb isotopic disturbance and resetting within zircon. In their specific example the length scale of disturbance was less than 10 μm (Carson et al., 2002) whereas in RI15 isotopic disturbance and resetting within zircon occurs on scales of 1–50 μm. This more extensive resetting may reflect higher fluid–rock ratios, syn-pegmatite shearing, or pre-conditioning of the zircons by earlier higher temperatures associated with the Prydz Event to make them more susceptible to attack and disturbance.

8.3. Implications for the use of zircon in dating high-grade metamorphism

The disequilibrium zircon–garnet REE relationships observed in RI15 indicate that the granulite facies events that led to garnet formation and its subsequent reaction to form the garnet–orthopyroxene–plagioclase–quartz assemblage are not those which led to the chemical modification and associated extensive Pb-loss in zircon at c. 510 Ma. Instead, as argued above zircon modification is attributed to fluid–rock interactions that progressed during the terminal phase of the Prydz tectonic event. The metamorphic events that formed and later partially replaced the garnet are not registered in the zircon age data as obtained from modified zircon domains.

This result has wider implications for the interpretation of zircon age data from modified protolith grains in rocks in which new zircon growth is limited. The conventional interpretation of disturbed zircon domains with extensive Pb loss and low Th/U is that these reflect metamorphism, and by implication yield the age of the peak metamorphic event. However, the evidence presented for this case study shows that such an assumption must be tested using complementary chemical evidence linked to textural analysis. The age given by the reset zircons may, of course, be close to or within error of the age of the overprinting peak metamorphic event if that event is short in duration and terminated rapidly, as may be the case with the Prydz tectonic event. However, where two or more granulite events have occurred, or where the *P–T* evolution is long lived and characterised by slow near-isobaric cooling (e.g. at d*T*/d*t* of 1–4 °C/Myr) the age of peak metamorphism may be poorly constrained or even unconstrained by the zircon data. In the Rauer Islands case study the zircon age data obtained from RI15, interpreted in the light of the REE systematics, do not resolve whether the granulite assemblage formed in the Archaean, in the Rauer tectonic event at 1030–990 Ma (Kinny et al., 1993) or early in the Prydz tectonic event (e.g. at 530–510 Ma; Fitzsimons, 2000). Hence, the question of whether the Archaean of the Rauer Islands experienced only the Prydz tectonic event (Hensen and Zhou, 1997) or was interleaved with the Mesoproterozoic gneisses of the area during the c. 1000 Ma Rauer tectonic event (e.g. Harley et al., 1995) remains an open one that requires testing using other gneisses from the Archaean domain.

9. Conclusions

The chemical response of zircon in essentially dry igneous rocks to the imposition of overprinting metamorphic events at even high grades of >800–830 °C may be weak or negligible, such that these metamorphic events are poorly recorded, if at all, in the zircon U–Pb age data. On the other hand, the chemical and isotopic sensitivity of zircon to fluid-activated or -mediated processes is likely to lead to extensive Pb-loss and age resetting on microns to several tens of microns scales within zircon grains, potentially causing misinterpretation of the event significance of the recorded ages.

The use of Y and REE distribution data for zircon and garnet allows the zircon ages in such chemically modified and texturally disturbed zircon micro-domains to be assessed and interpreted with considerably more confidence. Zircon that has been modified and isotopically reset during a metamorphic event in which garnet is growing, and which is potentially in chemical communication with this garnet, will exhibit a change in its REE composition so as to approach or attain REE equilibrium with the metamorphic garnet. This equilibrium signature can be assessed simply by comparing the measured zircon–garnet REE distribution, D_{REE}(zrc/grt), with those previously inferred in the literature to represent equilibrium. Even though there is uncertainty over which D_{REE}(zrc/grt) represent equilibrium (e.g. Harley et al., 2001; Whitehouse and Platt, 2003; Rubatto, 2002), in all cases the *change* in zircon MREE and HREE from undisturbed original zircon domains to disturbed/modified zircon

approaching equilibrium with garnet is predictable and can be used to evaluate the timing of zircon modification with respect to garnet formation and even reaction, as accomplished here for the Rauer Islands example. In this case the isotopically reset and chemically modified former magmatic zircons show changes in their MREE contents and chondrite normalised patterns that are inconsistent with equilibration with the abundant garnet in the rock, or with its reaction products, but instead reflect a zircon response to fluid interaction at c. 510 Ma that post-dates the granulite facies mineral assemblage evolution of RI15 and by implication of the Rauer Islands as a whole.

Acknowledgements

SLH thanks ANARE for logistic and field support on the 1992–1993 field season in which the rock samples were collected, I. Snape for access to his unpublished PhD thesis data, and L.P. Black for provision of the SHRIMP polished mount of RI15 and RI43. R.W. Hinton, D. Steele and the EMMAC ion microprobe team at Edinburgh provided invaluable support with micro-analysis. Joe Pyle and Daniella Rubatto are thanked for their positive and useful reviews. This research is supported by NERC grant NE/B504157/1 to SLH.

Appendix A. Supplementary data

Supplementary data associated with this article can be found, in the online version, at doi:10.1016/j.chemgeo.2007.02.011.

References

Anders, E., Grevasse, N., 1989. Abundances of the elements — meteoritic and solar. Geochim. Cosmochim. Acta 53, 197–214.

Aranovich, L.Y., Berman, R.G., 1997. A new garnet–orthopyroxene thermometer based on reversed Al_2O_3 solubility in $FeO–Al_2O_3–SiO_2$ orthopyroxene. Am. Mineral. 82, 345–353.

Boger, S.D., Wilson, C.J.L., Fanning, C.M., 2001. Early Palaeozoic tectonism within the east Antarctic craton: the final suture between east and west Gondwana? Geology 29, 463–466.

Carson, C.J., Fanning, C.M., Wilson, C.J.L., 1996. Timing of the Progress Granite, Larsemann Hills, evidence for Early Palaeozoic orogenesis within the East Antarctic Shield and implications for Gondwana assembly. Aust. J. Earth Sci. 43, 539–553.

Carson, C.J., Ague, J.J., Grove, M., Coath, C.D., Harrison, T.M., 2002. U–Pb isotopic behaviour of zircon during upper-amphibolite facies fluid infiltration in the Napier Complex, east Antarctica. Earth Planet. Sci. Lett. 199, 287–310.

Corfu, F., Hanchar, J.M., Hoskin, P.W.O., Kinny, P., 2003. Atlas of zircon textures. In: Hanchar, J.M., Hoskin, P.W.O. (Eds.), Reviews in Mineralogy and Geochemistry, vol. 53. Mineralogical Society of America, Washington, pp. 469–495. Zircon.

Degeling, H., Eggins, S., Ellis, D.J., 2002. Zr budgets for metamorphic reactions, and the formation of zircon from garnet breakdown. Min. Mag. 65, 749–758.

Fitzsimons, I.C.W., 2000. A review of tectonic events in the East Antarctic Shield and their implications for Gondwana and earlier supercontinents. J. Afr. Earth Sci. 31, 3–23.

Fraser, G., Ellis, D., Eggins, S., 1997. Zirconium abundance in granulite-facies minerals, with implications for zircon geochronology in high-grade rocks. Geology 25, 607–610.

Friend, C.R.L., Kinny, P.D., 1995. New evidence for protolith ages of Lewisian granulites, northwest Scotland. Geology 23, 1027–1030.

Friend, C.R.L., Nutman, A.P., 1992. Response of zircon U–Pb isotopes and whole rock geochemistry to CO_2 fluid-induced granulite-facies metamorphism, Kabbaldurga, Karnataka, South India. Contrib. Mineral. Petrol. 111, 299–310.

Ganguly, J., Cheng, W., Tirone, M., 1996. Thermodynamics of aluminosilicate garnet solid solution; new experimental data, an optimised model, and thermometry applications. Contrib. Mineral. Petrol. 126, 137–151.

Hanchar, J.M., Miller, C.F., 1993. Zircon zonation patterns as revealed by cathodoluminescence and backscattered electron images: implications for interpretation of complex crustal histories. Chem. Geol. 110, 1–13.

Harley, S.L., 2003. Archaean–Cambrian development of East Antarctica: metamorphic characteristics and tectonic implications. In: Yoshida, M., Windley, B.F. (Eds.), Proterozoic East Gondwana: Supercontinent Assembly and Breakup Spec. Publ. Geol. Soc. Lond., vol. 206, pp. 203–230.

Harley, S.L., Black, L.P., 1997. A revised Archaean chronology for the Napier Complex, Enderby Land, from SHRIMP ion-microprobe studies. Antarct. Sci. 9, 74–91.

Harley, S.L., Fitzsimons, I.C.W., 1995. High-grade metamorphism and deformation in the Prydz Bay region, East Antarctica: terranes, events and regional correlations. In: Yoshida, M., Santosh, M. (Eds.), India and Antarctica during the Precambrian. Mem. Geol. Soc. India, vol. 34, pp. 73–100.

Harley, S.L., Snape, I., Fitzsimons, I.C.W., 1995. Regional correlations and terrane assembly in East Prydz Bay: evidence from the Rauer Group and Vestfold Hills. Terra Antartica 2, 49–60.

Harley, S.L., Snape, I., Black, L.P., 1998. The evolution of a layered metaigneous complex in the Rauer Group, East Antarctica: evidence for a distinct Archaean terrane. Precambrian Res. 89, 175–205.

Harley, S.L., Kinny, P.D., Snape, I., Black, L.P., 2001. Zircon chemistry and the definition of events in Archaean granulite terrains. In: Cassidy, K.F., Dunphy, J.M., van Kranendonk, M.J. (Eds.), Extended Abstracts of 4th International Archaean Symposium. AGSO-Geoscience Australia Record 2001/37, Canberra, pp. 511–513.

Hartmann, L.A., Takehara, L., Leite, J.A.D., McNaughton, N.J., Vasconcellos, M.A.Z., 1997. Fracture sealing in zircon as evaluated by electron microprobe analyses and back-scattered electron imaging. Chem. Geol. 141, 67–72.

Hensen, B.J., Zhou, B., 1995. A Pan-African granulite facies metamorphic episode in Prydz Bay, Antarctica: evidence from Sm–Nd garnet dating. Aust. J. Earth Sci. 42, 249–258.

Hensen, B.J., Zhou, B., 1997. East Gondwana amalgamation by Pan-African collision? Evidence from Prydz Bay, Eastern Antarctica. In: Ricci, C.A. (Ed.), The Antarctic Region: Geological Evolution and Processes. Terra Antartica Publication, Siena, pp. 115–119.

Hinton, R.W., Upton, B.G.J., 1991. The chemistry of zircon: variations within and between large crystals from syenite and alkali basalt xenoliths. Geochim. Cosmochim. Acta 55, 3287–3302.

Hoskin, P.W.O., Black, L.P., 2000. Metamorphic zircon formation by solid state recrystallisation of protolith igneous zircon. J. Metamorph. Geol. 18, 423–439.

Kelly, N.M., Harley, S.L., 2005. An integrated microtextural and chemical approach to zircon geochronology: refining the Archaean history of the Napier Complex, east Antarctica. Contrib. Mineral. Petrol. 149, 57–84.

Kinny, P.D, Black, L.P., Sheraton, J.W., 1993. Zircon ages and distribution of Archaean and Proterozoic rocks in the Rauer Islands. Antarct. Sci. 5, 193–206.

Koschek, G., 1993. Origin and significance of SEM cathodoluminescence from zircon. J. Microsc. 171, 223–232.

Ludwig, K.R., 1999. User manual for Isoplot/Ex, version 2.10, a geochronological toolkit for Microsoft Excel. Berkley Geochronological Centre Special Publication 1a.

Ludwig, K.R., 2001. Squid v1.02 — a user's manual. Berkeley Geochronological Centre Special Publication No. 2, p. 19.

McLaren, A.C., Fitzgerald, J.D., Williams, I.S., 1994. The microstructure of zircon and its influence on the age determination of Pb/U isotopic ratios measured by ion microprobe. Geochim. Cosmochim. Acta 58, 993–1005.

Pidgeon, R.T., 1992. Recrystallisation of oscillatory zoned zircon: some geochronological and petrological implications. Contrib. Mineral. Petrol. 110, 463–472.

Pidgeon, R.T., Nemchin, A.A., Hitchen, J.G., 1998. Internal structures of zircons from Archaean granites from the Darling Range batholith: implications for zircon stability and the interpretation of zircon U–Pb ages. Contrib. Mineral. Petrol. 132, 288–299.

Pouchou, L., Pichoir, F., 1984. A new model for quantitative X-ray microanalysis. Res. Aeros. 3, 167–192.

Roberts, M.P., Finger, F., 1997. Do U–Pb zircon ages from granulites reflect peak metamorphic conditions? Geology 25, 319–322.

Rubatto, D., 2002. Zircon trace element geochemistry: partitioning with garnet and the link between U–Pb ages and metamorphism. Chem. Geol. 184, 123–138.

Rubatto, D., Williams, I.S., Buick, I.S., 2001. Zircon and monazite response to prograde metamorphism in the Reynolds Range, central Australia. Contrib. Mineral. Petrol. 140, 458–468.

Schaltegger, U., Fanning, C.M., Günther, D., Maurin, J.C., Schulmann, K., Gebauer, D., 1999. Growth, annealing and recrystallisation of zircon and preservation of monazite in high-grade metamorphism: conventional and in-situ U–Pb isotope, cathodoluminescence and microchemical. Contrib. Mineral. Petrol. 134, 186–201.

Sims, J.R., Dirks, P.H.G.M., Carson, C.J., Wilson, C.J.L., 1994. The structural evolution of the Rauer Group, East Antarctica: mafic dykes as passive markers in a composite Proterozoic terrain. Antarct. Sci. 6, 379–394.

Snape, I., 1997. Geological and geochemical anatomy of Archaean gneisses from the Vestfold Hills and Rauer Group, East Antarctica. Unpubl. Ph.D. thesis, University of Edinburgh.

Valley, J.W., Graham, C.M., Harte, B., Eiler, J., Kinny, P.D., 1998. In: McKibben, M.A., Shanks III, W.C., Ridley, W.I. (Eds.), Applications of Microanalysis in Understanding Mineralizing Processes, pp. 73–98.

van Westrenen, W., Blundy, J., Wood, B.J., 1999. Crystal–chemical controls on trace element partitioning between garnet and anhydrous silicate melt. Am. Mineral. 84, 838–847.

Vavra, G., Gebauer, D., Schmid, R., Compston, W., 1996. Multiple zircon growth and recrystallisation during polyphase Late Carboniferous to Triassic metamorphism in granulites of Ivrea Zone (Southern Alps): an ion microprobe (SHRIMP) study. Contrib. Mineral. Petrol. 122, 337–358.

Vavra, G., Schmid, R., Gebauer, D., 1999. Internal morphology, habit and U–Th–Pb microanalysis of amphibolite-to-granulite facies zircons: geochronology of the Ivrea Zone (Southern Alps). Contrib. Mineral. Petrol. 143, 380–404.

Whitehouse, M.J., Platt, J.P., 2003. Dating high-grade metamorphism — constraints from rare-earth elements in zircon and garnet. Contrib. Mineral. Petrol. 145, 61–74.

Zhao, Y., Liu, X., Song, B., Zhang, Z., Li, J., Yao, Y., Wang, Y., 1995. Constraints on the stratigraphic age of metasedimentary rocks from the Larsemann Hills, East Antarctica: possible implications for Neoproterozoic tectonics. Precambrian Res. 75, 175–188.